2014-08-03

# Optical Beam Propagation in Oceanic Turbulence

Nathan Farwell
*University of Miami*, nathanfarwell@gmail.com

Follow this and additional works at: https://scholarlyrepository.miami.edu/oa_dissertations

UNIVERSITY OF MIAMI


OPTICAL BEAM PROPAGATION IN OCEANIC TURBULENCE


By

Nathan Farwell


A  DISSERTATION


Submitted to the Faculty
of the University of Miami
in partial fulfillment of the requirements for
the degree of Doctor of Philosophy


Coral Gables, Florida

August 2014

UNIVERSITY OF MIAMI


A dissertation submitted in partial fulfillment of
the requirements for the degree of
Doctor of Philosophy


OPTICAL BEAM PROPAGATION IN OCEANIC TURBULENCE


Nathan Farwell


Approved:


_____
Olga Korotkova, Ph.D.
Associate Professor of Physics

_____
Kenneth Voss, Ph.D.
Professor of Physics


_____
Howard Gordon, Ph.D.
Distinguished Professor of Physics

_____
Weilin Hou, Ph.D.
Oceanographer
US Naval Research Lab
Stennis Space Center,
Mississippi


_____
Svetlana Avramov-Zamurovic, Ph.D.
Professor, Weapons and Systems Engineering
US Naval Academy
Annapolis, Maryland

_____
M. Brian Blake, Ph.D.
Dean of the Graduate School

FARWELL, NATHAN                                        (Ph.D., Physics)
Optical Beam Propagation in Oceanic Turbulence              (August 2014)

Abstract of a dissertation at the University of Miami.

Dissertation supervised by Professor Olga Korotkova.
No. of pages in text. (72)

Optical beam propagation through oceanic waters is explored using a recently proposed model for the refractive index fluctuations in oceanic turbulence. The model provides an accurate depiction of the ocean through the inclusion of both temperature and salinity fluctuations to the index of refraction. Beam characteristics of fundamental importance to communication links, remote sensing, and laser radar links are explored including intensity, degree of coherence, and scintillation.  Theoretical values of these parameters are found through the use of classical Rytov theory and compared to those found using a numerical optics random phase screen simulation. The impact of the oceanic turbulence is compared with that found in atmospheric turbulence as well as other random media such as biological tissue. The results presented serve as a foundation for the study of optical beam propagation in oceanic turbulence comparable to the widely studied area of propagation through atmospheric turbulence.

# Contents

# List of Figures

viii

# Chapter 1

# Introduction

The study of light propagation through random media is a perpetually important topic for its many applications in the atmosphere, biological tissues, and the ocean. While much has been done both theoretically and experimentally in the atmosphere and in bio-tissues, the ocean has not received as much attention. This text explores optical beam propagation through ocean waters using a recent optical turbulence model that incorporates contributions from both temperature and salinity [1]. In the study, scattering and absorption by particles are not considered, but instead the focus is on the effects of optical turbulence alone. In Chapter 1 the oceanic turbulence to be studied is characterized alongside a review of traditional optical turbulence theory and the extension into the oceanic model. Chapter 2 outlines traditional approaches to beam propagation through turbulence, such as the Rytov small perturbation method and the extended Huygens-Fresnel integral method, including free space propagation. The following chapters use these methods to investigate the beam propagation through the ocean in terms of its scintilllation, average intensity, and coherence in Chapter 3. Chapter 4 deals with the changes in the spectrum of a scalar stochastic beam followed by an investigation into the polarization properties
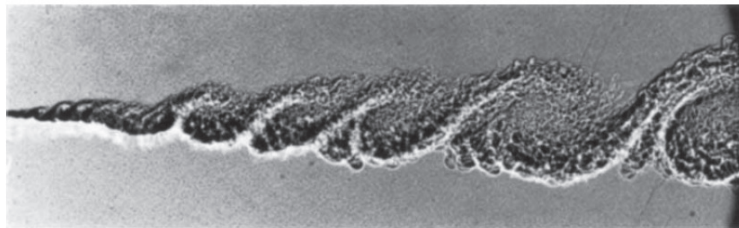
Figure 1.1: Cascade of energy from large-scale turbulent eddies to small-scale eddies in a turbulent mixture. From Ref. [2]

of an electromagnetic stochastic beam on propagation through oceanic turbulence in Chapter 5. A numerical multiple phase screen simulation is used in Chapter 6 as an alternative method to investigate intensity and scintillation properties of a coherent beam transmitted through oceanic turbulence followed by concluding statements in Chapter 7.

## 1.1   Oceanic Turbulence

The ocean, much like the atmosphere, is in a constant state of irregular and highly unpredictable motion throughout. It is by nature a chaotic process that complicates the understanding of all aspects of the ocean. We can however identify several intrinsic characteristics of the ocean that will enable us to describe and ultimately quantify the turbulence in all areas, from just beneath the surface to great depths.

We will start with the idea that the energy necessary for the turbulent mixing in the ocean is supplied at a large scale, creating large scale eddies. These large eddies go on to "cascade", or disperse their energy into smaller and smaller eddies until finally dissipating their kinetic energy into heat. Figure 1.1 shows this structure of

small-scale eddies forming out of large-scale eddies. This figure also highlights the question that the turbulence may have some anisotropy in the larger scaled eddies. When the energy is provided for the turbulence as a result of, among other things, tidal forces from the gravitational attraction of the Moon and Sun, atmospheric interaction at the surface, and even geothermal vents in the deep ocean, it can have some directional asymmetry. It has been found in practice that this asymmetry is diminished as eddies interact with one another, and cascade their energy, yielding many regions of the ocean that do show isotropic turbulence [7]. We will use this assumption of isotropic turbulence, as is common in the study of the atmosphere as well, from this point forward.

A further important assumption necessary for our analysis is that our turbulence can be characterized without the need for any time dependence through the use of the Taylor's hypothesis of frozen turbulence. This hypothesis states that as eddies are transported past a fixed point, they remain fundamentally unchanged, or frozen. With this in mind, we can evaluate the time taken for eddies of different sizes to pass by a fixed point and translate that time into spatial measurements of wavenumbers of the eddies, given by $k_e = 2\pi/l$ with $l$ being the size of the eddy, through the average velocity of the motion. With $T = l/V$ being the time it takes for an eddy of size $l$ to pass a fixed point, and its corresponding frequency $\sigma = 2\pi/T$, one can substitute in to find a spatial frequency given by $\sigma_r = kV$. From here we are able to see that the influence of differently-sized turbulent eddies can be directly related to velocity fluctuations without an explicit time dependence. It was Kolmogorov who first showed that the energy of homogeneous and isotropic turbulence is distributed

as a function of the wavenumber of eddies. Using that, along with a dimensional analysis of the velocity fluctuations, he was able to describe the one-dimensional spectral kinetic energy density of the velocity fluctuations given by [3]

$$\Phi(\kappa) = q\epsilon^{2/3}\kappa^{-5/3}, \tag{1.1}$$

where $q$ is a non-dimensional constant and $\epsilon$ is the rate of dissipation of kinetic energy. It is from this equation that we establish a three-dimensional model for the power spectrum described in section 1.2 that serves as a basis for all other models that follow. We will show in detail in Chapter 2 how this spectrum, which gives the distribution of energy as a function of eddy size, allows us to analyze the propagation of an optical beam through the turbulence.

In our analysis, we will be interested in several additional characteristics of the ocean that will help us more accurately describe the turbulence. In particular we will be heavily interested in $\epsilon$, the rate of dissipation of kinetic energy, $\chi_T$, the rate of dissipation of mean squared temperature variance, and $w$, the density gradient ratio.

The dissipation of kinetic energy, $\epsilon$, is the dissipation of the kinetic energy per unit mass that is lost through viscosity to heat. In the case of isotropic turbulence, which we assume in our study, it can be written as [7]

$$\epsilon = (15/2)v\langle(\partial u/\partial z)^2\rangle, \tag{1.2}$$

where $v$ is the kinematic viscosity and $u$ is the velocity in the z-direction. Here the

z-direction is chosen for convenience, and functions to show that the derivative should be taken in only one direction, as all directions will be equal due to the isotropy. Practically, measurement of $\epsilon$ can be done with the assumption of isotropy and has values which range from $10^{-4} \, m^2/s^3$ in the most active turbulent regions of the ocean, to $10^{-10} \, m^2/s^3$ in the more calm, deep waters [8].

Paramter $\chi_T$ is a measure of the dissipation rate of temperature variance that, with the assumption of isotropic turbulence, is given by the expression

$$\chi_T = 6K_T \langle (\partial T'/\partial z)^2 \rangle, \tag{1.3}$$

where $T$ is temperature and $K_T$ is the eddy diffusivity of temperature. Parameter $\chi_T$ has been shown to vary on the range $10^{-4} \frac{K^2}{s}$ to $10^{-10} \frac{K^2}{s}$ [8]. Here the parameter $K_T$, representing the eddy diffusivity of temperature, has been introduced. This parameter not only appears in the derivation of $\chi_T$ but will be important later when the assumption is made that the eddy diffusivity of temperature and salt ($K_S$) are equal. This assumption has been widely used in many aspects of the measurement and interpretation of small-scale turbulence and its effects in the ocean and we will use it in our analysis as well. However, several recent studies have shown that it may not be appropriate in all cases [9], [10]. Although these studies do show that the ratios of eddy diffusivity of temperature and salinity may not be exactly equal in regions of weak turbulence, the assumption is appropriate in the regions of stronger turbulence investigated in the later chapters.

Finally, $w$ is the density gradient ratio given by [1]

$$w = \frac{\alpha(dT/dz)}{\beta(dS/dz)}, \tag{1.4}$$

where $\alpha = 2.6 \times 10^{-4}$ liters/degree and $\beta = 1.75 \times 10^{-4}$ liters/gram are the coefficients of expansion for temperature and salinity. This ratio of contributions of the vertical temperature and vertical salinity gradients to $w$, gives a value less than zero for the so called "doubly stable" regime that we will be interested in. This region is one where salinity increases with greater depth in the water while temperature decreases, which is the most common scenario. Typical values for $w$ in this region fall between $0$ and $-5$ with $0$ being heavily salinity dominated and $-5$ being heavily temperature dominated [1].

## 1.2   Optical Turbulence

When we speak about optical turbulence we are interested in the random index-of-refraction fluctuations that affect the beam as it travels through a medium. With knowledge of the properties of any given medium we aim to create a three dimensional power spectrum for the optical turbulence to use in our analysis. In the atmosphere these index-of-refraction fluctuations are commonly associated only with the small temperature changes caused by the constant motion as other properties are negligible in comparison. If we consider the random fluctuations to be statistically homogeneous and isotropic, the most well-known and widely used model for the atmosphere is the Kolmogorov
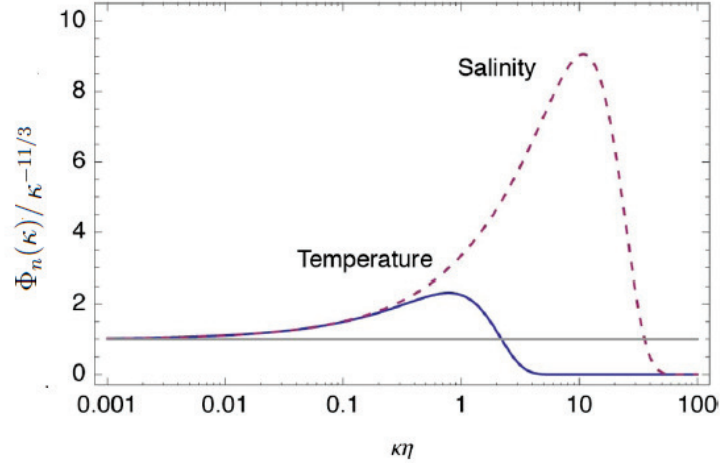
Figure 1.2: Power spectrum of the refractive index fluctuations in oceanic turbulence due to temperate fluctuations (solid curve) and salinity fluctuations (dashed curve) normalized by the Kolmogorov power law spectrum. From Ref. [6].

spectrum defined by the formula [3]

$$\Phi(\kappa) = 0.033C_n^2\kappa^{-11/3}. \tag{1.5}$$

This is the three-dimensional extension to the spectrum shown in equation 1.1. Here $C_n^2$ is the refractive index structure constant and $\kappa$ is the scalar spatial wave number. While this model is very good for analyzing the atmosphere, it does not feature the small rise in high wave numbers shown by Champagne et al. [4], and does not account for the salinity contributions necessary for oceanic studies.

Individual power spectra that include this high wave number "bump" for both temperature and salinity in the ocean have been known for some time [5], but it was only recently that an analytical model combining the two has appeared [1]. Figure 1.2 shows the individual spectra for temperature and salinity-based refractive

index fluctuations in the ocean normalized by the Kolmogorov power law spectrum highlighting the high wave number bump in each. A single spectrum accounting for both factors is crucial in our analysis of oceanic light propagation. With this model we assume clear water, that is to say we only are interested in optical turbulence effects, and will not consider absorption and scattering by particles. We also limit our discussion to the case where eddy thermal diffusivity $(K_T)$ and the diffusion of salt $(K_S)$ are equal. We then have [1]

$$\Phi_n(\kappa) = 0.388 \times 10^{-8} \varepsilon^{-1/3} \kappa^{-11/3} [1 + 2.35(\kappa\eta)^{2/3}] f(\kappa, w, \chi_T), \qquad (1.6)$$

where $\eta$ is the Kolmogorov micro scale (inner scale). Here also

$$f(\kappa, w, \chi_T) = \frac{\chi_T}{w^2} \left( w^2 e^{-A_T\delta} + e^{-A_S\delta} - 2we^{-A_{TS}\delta} \right),$$

with $A_T = 1.863 \times 10^{-2}$, $A_S = 1.9 \times 10^{-4}$, $A_{TS} = 9.41 \times 10^{-3}$, and $\delta = 8.284(\kappa\eta)^{4/3} + 12.978(\kappa\eta)^2$. Figure 1.3 shows a plot of the spectrum defined in equation 1.6 normalized by the Kolmogorov power law spectrum. Here we highlight the effect of $w$, the parameter relating the relative strength of temperature and salinity fluctuations on the shape of the spectrum. Parameters $\chi_T$ and $\varepsilon$ are not shown but contribute to the relative height of the spectrum.
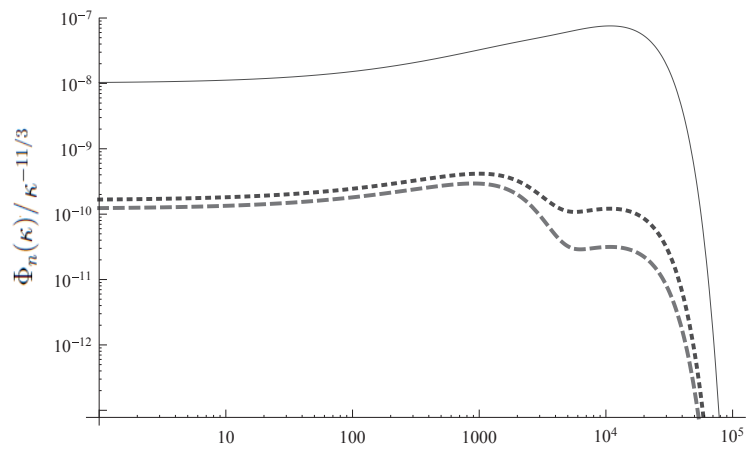
Figure 1.3: Log-log plot of the oceanic power spectrum $\Phi_n(\kappa)$, calculated from Eq. 1.6 and normalized by the Kolmogorov power-law $\kappa^{-11/3}$, for $w = -0.1$ (solid curve), $w = -2.5$ (dotted curve), $w = -4.9$ (dashed curve).

# Chapter 2

# Beam Propagation Through Random Media

## 2.1  Scalar Beam Propagation Theory

The equation governing the propagation of one of the scalar components of the electric field with wavelength $\lambda$, denoted by $U(\mathbf{r}, \lambda)$, into the half-plane $z > 0$, is the scalar stochastic Helmholtz equation [11]

$$\nabla^2 U(\mathbf{r}, z) + k^2 n^2(\mathbf{r}, z) U(\mathbf{r}, z) = 0, \tag{2.1}$$

where $n(\mathbf{r}, z)$ is the index of refraction, $k = 2\pi/\lambda$ is the wave number and $\mathbf{r}$ is a vector in the plane perpendicular to propagation, which for our case will be the x-y axis as shown in Figure 2.1. The explicit dependence of $U(\mathbf{r}, z)$ on the wavelength $\lambda$ has been omitted for brevity where appropriate. Beginning with the case of free space propagation, where in this equation $n(\mathbf{r}, z) = 1$, we can make the usual paraxial, or small-angle approximation that leads to the paraxial wave equation [11]

$$\frac{1}{r}\frac{\partial}{\partial r}\left(r\frac{\partial V(\mathbf{r}, z)}{\partial r}\right) + 2ik\frac{\partial V(\mathbf{r}, z)}{\partial z} = 0, \tag{2.2}$$
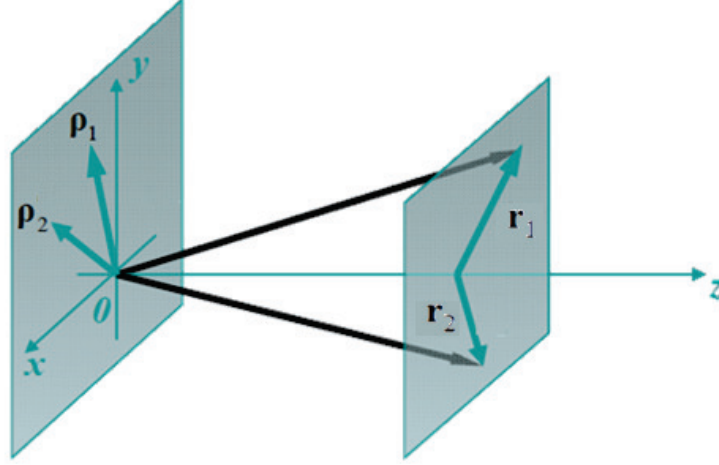
Figure 2.1: A graphical description of the vector geometry associated with propagation throughout the paper

where $V(\mathbf{r}, z) = U(\mathbf{r}, z) \exp[-ikz]$ and $i$ is the unit imaginary number. One solution to the paraxial wave equation is through the Huygens-Fresnel integral approach. This solution takes the form of the field at a distance $z$ along its propagation path $U(\mathbf{r}, z)$ given by

$$U(\mathbf{r}, z) = -2ik \iint_{-\infty}^{\infty} G(\boldsymbol{\rho}, \mathbf{r}, z) U(\boldsymbol{\rho}, 0) d^2\rho, \tag{2.3}$$

where $U(\boldsymbol{\rho}, 0)$ is the field in the source plane, and $G(\boldsymbol{\rho}, \mathbf{r}, z)$ is the free-space Green's function, which under the paraxial approximation is given by the expression

$$G(\boldsymbol{\rho}, \mathbf{r}, z) = \frac{1}{4\pi z} \exp[ikz + \frac{ik}{2z}|\boldsymbol{\rho} - \mathbf{r}|^2]. \tag{2.4}$$

Here $\boldsymbol{\rho}$ is a vector in the source plane as shown in Figure 2.1.

When we do include random fluctuations in the index of refraction it is possible to solve Equation 2.1 resulting in the extended Huygens-Fresnel integral [11]. In this

case we find that

$$U(\mathbf{r}, z) = -\frac{ik}{2\pi z} \exp[ikz] \iint_{-\infty}^{\infty} U(\boldsymbol{\rho}, 0) \exp[\frac{ik|\boldsymbol{\rho} - \mathbf{r}|^2}{2z} + \psi(\mathbf{r}, \boldsymbol{\rho})] d^2\rho, \qquad (2.5)$$

with $\psi(\mathbf{r}, \boldsymbol{\rho})$ being the random part of the complex phase of a spherical wave propagating in the turbulent medium.

While it has been shown that equation 2.5 is valid for the first and second-order field moments under weak or strong fluctuations of the medium, it has not been demonstrated that it is accurate for the fourth-order moment. These moments of the field are what allows us to investigate the ensemble averaged properties of the beam we will be interested in later. The second moment will allow us to calculate both the average intensity distribution of the beam, and its degree of coherence while the fourth order moment enables us to calculate the scintillation index essential for applications such as communication links and laser radar links. Moreover, the scintillation index conventionally serves as a tool for separating the regimes of weak and strong fluctuations in the medium and determines which propagation methods can be employed for certain links. Due to this, we shall turn our attention to another solution to equation 2.1 with fluctuations in the index of refraction included given by the Rytov approximation that will allow us to calculate the fourth moment as well.

## 2.2    Rytov Approximation

The method for solving equation 2.1 using a perturbational approach developed by

Rytov [12] has been applied to the problem of wave propagation in random media

as early as 1953 [13], [54]. Following the classical Rytov method we assume that the

field at a distance $L$ from the source can be represented by the series [11]

$$U(\mathbf{r}, L) = U_0(\mathbf{r}, L) \exp[\psi(\mathbf{r}, L)]$$
$$= U_0(\mathbf{r}, L) \exp[\psi_1(\mathbf{r}, L) + \psi_2(\mathbf{r}, L) + ...], \tag{2.6}$$

with $U_0(\mathbf{r}, L)$ being the result of free-space propagation of the initial beam field given

through the Huygen-Fresnel integral, (see equation 2.3), and $\psi(\mathbf{r}, L)$ representing the

total complex phase perturbation of the field due to the optical turbulence. $\psi_1(\mathbf{r}, L)$

and $\psi_2(\mathbf{r}, L)$ are then first and second-order perturbations, respectively.

With this representation, we can begin to investigate the second and fourth-order

statistics of our propagated beams. The second-order correlation function, or cross-spectral

density, of the scalar field $U$ is defined as

$$W_2(\mathbf{r}_1, \mathbf{r}_2, z) = \langle U^*(\mathbf{r}_1, z) U(\mathbf{r}_2, z) \rangle$$
$$= \iint U^*(\boldsymbol{\rho}_1, z) U(\boldsymbol{\rho}_2, z) K(\mathbf{r}_1, \mathbf{r}_2, \boldsymbol{\rho}_1, \boldsymbol{\rho}_2, z) d^2\rho_1 d^2\rho_2, \tag{2.7}$$

where the brackets denote the ensemble average over the realizations of the random

medium and $^*$ denotes the complex conjugate. Here $\boldsymbol{\rho}_1$ and $\boldsymbol{\rho}_2$ are vectors in the

source plane and the propagator $K$ is derived from the free-space Green's function

as in equation 2.4 as well as including the correlation function of the complex phase
and takes the form [11]

$$K(\mathbf{r}_1, \mathbf{r}_2, \boldsymbol{\rho}_1, \boldsymbol{\rho}_2, z) = (\frac{k}{2\pi z})^2 \exp[-ik\frac{(\mathbf{r}_1 - \boldsymbol{\rho}_1)^2 - (\mathbf{r}_2 - \boldsymbol{\rho}_2)^2}{2z}]$$
$$\times \langle \exp[\psi^*(\mathbf{r}_1, \boldsymbol{\rho}_1, z) + \psi(\mathbf{r}_1, \boldsymbol{\rho}_2, z)]\rangle_m. \tag{2.8}$$

The correlation function of the complex phase, $\langle \exp[\psi^*(\mathbf{r}_1, \boldsymbol{\rho}_1, z) + \psi(\mathbf{r}_1, \boldsymbol{\rho}_2, z)]\rangle_m$
will be solved explicitly in later chapters for different sources. When considering
an electromagnetic field, the cross-spectral density $W_2$ must be extended to a $2 \times 2$
matrix $W_{2,ij}$ given by the formula

$$W_{2,ij}(\mathbf{r}_1, \mathbf{r}_2, z) = \langle E_i(\mathbf{r}_1, z)E_j(\mathbf{r}_2, z)\rangle, \tag{2.9}$$

where $E_x$ and $E_y$ are the mutually orthogonal components of the electric field.

Returning to the scalar case, with the expression for the cross-spectral density in
hand, we find that to solve for the average intensity at a given position, we need to
evaluate $W_2$ at the same position for both arguments, that is $\mathbf{r}_1 = \mathbf{r}_2 = \mathbf{r}$, giving us
[11]

$$I(\mathbf{r}, z) = W_2(\mathbf{r}, \mathbf{r}, z). \tag{2.10}$$

At this point we are also prepared to calculate the complex degree of coherence defined
as

$$\mu(\mathbf{r}_1, \mathbf{r}_2, z) = \frac{W_2(\mathbf{r}_1, \mathbf{r}_2, z)}{\sqrt{W_2(\mathbf{r}_1, \mathbf{r}_1, z)W_2(\mathbf{r}_2, \mathbf{r}_2, z)}} = \frac{W_2(\mathbf{r}_1, \mathbf{r}_2, z)}{\sqrt{I(\mathbf{r}_1, z)I(\mathbf{r}_2, z)}}. \tag{2.11}$$

The complex degree of coherence is a measure of the statistical similarity of the light

field at two points $\mathbf{r}_1$ and $\mathbf{r}_2$ that falls between $0 <= |\mu(\mathbf{r}_1, \mathbf{r}_2, z)| <= 1$. For the lower

bound of 0 the light is said to be completely incoherent, as opposed to case of fully

coherent light when $|\mu(\mathbf{r}_1, \mathbf{r}_2, z)| = 1$.

It will also be important to analyze the fourth-order statistics, in particular the

scintillation index, which is the normalized variance of intensity fluctuations, through

the use of the fourth order cross-coherence function given by

$$W_4(\mathbf{r}_1, \mathbf{r}_2, \mathbf{r}_3, \mathbf{r}_4, z) = \langle U(\mathbf{r}_1, z)U^*(\mathbf{r}_2, z)U(\mathbf{r}_3, z)U^*(\mathbf{r}_4, z) \rangle, \tag{2.12}$$

which can be expressed as

$$\begin{aligned} W_4(\mathbf{r}_1, \mathbf{r}_2, \mathbf{r}_3, \mathbf{r}_4, z) &= U_0(\mathbf{r}_1, z)U_0^*(\mathbf{r}_2, z)U_0(\mathbf{r}_3, z)U_0^*(\mathbf{r}_4, z) \\ &\times \langle \exp[\psi(\mathbf{r}_1, z) + \psi^*(\mathbf{r}_2, z) + \psi(\mathbf{r}_3, z) + \psi^*(\mathbf{r}_4, z)] \rangle \end{aligned} \tag{2.13}$$

Again, the exact evaluations of the correlation of complex phase fluctuations will be

done later for specific sources. Using this, we can define the scintillation index as

$$\sigma_I^2(\mathbf{r}, z) = \frac{\langle I^2(\mathbf{r}, z) \rangle - \langle I(\mathbf{r}, z) \rangle^2}{\langle I(\mathbf{r}, z) \rangle^2}, \tag{2.14}$$

where again $I(\mathbf{r}, z)$ is given by equations 2.10 and $\langle I^2(\mathbf{r}, z) \rangle$ is the second moment of

the irradiance found by setting $\mathbf{r}_1 = \mathbf{r}_2 = \mathbf{r}_3 = \mathbf{r}_4 = \mathbf{r}$ in the fourth order coherence

function, equation 2.12, that is

$$\langle I^2(\mathbf{r}, z) \rangle = W_4(\mathbf{r}, \mathbf{r}, \mathbf{r}, \mathbf{r}, z) \tag{2.15}$$

## 2.3 Beam Sources

In our analysis we will investigate the effect of oceanic turbulence on several different beam sources. The most basic source examined in Chapter 3, is a scalar unit-amplitude Gaussian beam that at the source plane $z = 0$ is defined as

$$z = 0; \quad U_0(\boldsymbol{\rho}, 0) = \exp(-\frac{\rho^2}{W_0^2} - \frac{ik\rho^2}{2F_0}), \tag{2.16}$$

where $W_0$ and $F_0$ are the beam radius and phase front radius of curvature, respectively. We will investigate this beam starting with its scintillation properties and go on to investigate intensity and coherence as well.

The second beam source we will encounter is the scalar Gaussian Schell-Model beam with an explicit dependence on wavelength defined by its cross spectral density in the source plane as

$$W_{2,0}(\boldsymbol{\rho}_1, \boldsymbol{\rho}_2; \lambda) = \mathcal{I}_0(\lambda) \exp\left[-\frac{\rho_1^2 + \rho_2^2}{4\sigma^2}\right] \exp\left[-\frac{(\boldsymbol{\rho}_1 - \boldsymbol{\rho}_2)^2}{2\delta^2}\right], \tag{2.17}$$

Here $\mathcal{I}_0$ is the initial spectral composition consisting of a single Gaussian spectral line, i.e.

$$\mathcal{I}_0(\lambda) = \exp\left[-(\lambda - \lambda_0)^2/(2\Pi^2)\right], \tag{2.18}$$

which is centered at wavelength $\lambda_0$ with an r.m.s. width of $\Pi$. In addition we have that $\sigma$ is the r.m.s. width of the intensity, and $\delta$ is the r.m.s. width of the correlation function. This beam has a source plane intensity and degree of coherence that both

have Gaussian forms where the initial intensity is

$$I_0(\boldsymbol{\rho}_1, \boldsymbol{\rho}_2, \lambda) = \mathcal{I}_0(\lambda) \exp\left[-\frac{\boldsymbol{\rho}_1^2 + \boldsymbol{\rho}_2^2}{4\sigma^2}\right], \tag{2.19}$$

and the initial degree of coherence is seen to be

$$\mu_0(\boldsymbol{\rho}_1, \boldsymbol{\rho}_2) = \exp\left[-\frac{(\boldsymbol{\rho}_1 - \boldsymbol{\rho}_2)^2}{2\delta^2}\right]. \tag{2.20}$$

The two limiting cases of such a beam with respect to its coherence are when $\sigma << \delta$ giving a fairly coherent beam, and $\sigma >> \delta$ giving a nearly incoherent beam.

The final beam source we will use in our investigation is the electromagnetic version of the Gaussian Schell-model source (EMGSM) that will consider both the x and y components of the field. This vectorial generalization of the scalar Gaussian Schell-model beam has been studied extensively in previous literature for both free space [23]-[26], and in atmospheric turbulence [27]-[28].

We start by defining the cross spectral density matrix of an EMGSM beam at two points in the source plane, $\boldsymbol{\rho}_1$ and $\boldsymbol{\rho}_2$, by

$$W_{2,ij}(\boldsymbol{\rho}_1, \boldsymbol{\rho}_2, 0) = A_i A_j B_{ij} \exp\left[-\left(\frac{\boldsymbol{\rho}_1^2}{4\sigma_i^2} + \frac{\boldsymbol{\rho}_2^2}{4\sigma_j^2}\right)\right] \exp\left[-\frac{(\boldsymbol{\rho}_1 - \boldsymbol{\rho}_2)^2}{2\delta_{ij}^2}\right], \quad (i, j = x, y), \tag{2.21}$$

Here $A_i$ are the spectral amplitudes, $B_{ij}$ are the correlation coefficients of the x and y components, $\sigma_{i,j}$ is the r.m.s width of the intensity along the x and y components, and $\delta_{i,j}$ are the r.m.s. widths of the correlation functions of the x and y components.

All of these parameters are assumed to be independent of position.

To create a physically realizable EMGSM beam we must impose certain restrictions on these parameters. Following [29], section 4.3.2, we find that

$$B_{xx} = B_{yy} \equiv 1, \tag{2.22}$$

due to the fact that the diagonal components of the matrix represent the scalar cross spectral density functions. We also find from the quasi-Hermiticity property of the cross-spectral density matrix that [27],[30]

$$\delta_{xy} = \delta_{yx}, \tag{2.23}$$

$$B_{xy} = B_{yx}^*. \tag{2.24}$$

Further, as a result of the non-negative definite condition on the cross spectral density matrix, we must have as a necessary and sufficient condition [27]

$$|B_{xy}| \leq 1, \quad |B_{yx}| \leq 1. \tag{2.25}$$

It was shown in [24] that additionally a sufficient condition for a physically realizable field takes the form

$$\sqrt{\frac{\delta_{xx}^2 + \delta_{yy}^2}{2}} \leq \delta_{xy} \leq \sqrt{\frac{\delta_{xx}\delta_{yy}}{|B_{xy}|}}. \tag{2.26}$$

Finally, we find that in order to create a beam-like field, the diagonal elements of the

cross spectral density matrix must satisfy the inequalities [31]

$$\frac{1}{4\sigma_x^2} + \frac{1}{\delta_{xx}^2} << \frac{2\pi^2}{\lambda^2}, \quad \frac{1}{4\sigma_y^2} + \frac{1}{\delta_{yy}^2} << \frac{2\pi^2}{\lambda^2}. \tag{2.27}$$

Given that we have specified the source in terms of its cross spectral density we will need to modify the propagation equation 2.7 slightly giving for the scalar case

$$W_2(\mathbf{r}_1, \mathbf{r}_2; z, \lambda) = \int\int W_{2,0}(\boldsymbol{\rho}_1, \boldsymbol{\rho}_2; \lambda) K(\mathbf{r}_1, \mathbf{r}_2; \boldsymbol{\rho}_1, \boldsymbol{\rho}_2; z, \lambda) d^2\rho_1 d^2\rho_2, \tag{2.28}$$

and for the electromagnetic case

$$W_{2,ij}(\mathbf{r}_1, \mathbf{r}_2; z) = \int\int W_{ij}(\boldsymbol{\rho}_1, \boldsymbol{\rho}_2; 0) K(\mathbf{r}_1, \mathbf{r}_2; \boldsymbol{\rho}_1, \boldsymbol{\rho}_2; z) d^2\rho_1 d^2\rho_2, \quad (i,j = x, y),$$

$$\tag{2.29}$$

where in each formula, the propagator $K$ again follows from equation 2.8.

## 2.4 Strong Turbulence

To this point, the equations discussed are only valid in the regime of weak turbulence fluctuations. For the Gaussian beam, this regime is defined by restrictions on the parameter $q = L/k\rho_{pl}^2$ where $\rho_{pl}$ is the spatial coherence radius of a plane wave, i.e. the $1/e$ point of the degree of coherence at a propagation distance $L$. The inequalities

that define the strength of the turbulence have the form

$$q < 1 \quad \text{and} \quad q\Lambda < 1, \quad \text{(weak turbulence)},$$

$$q \gg 1 \text{ or } q\Lambda \gg 1, \quad \text{(strong turbulence)}.$$
(2.30)

It will become clear when investigating the scintillation properties, that it is necessary in the case of oceanic turbulence to extend this theory into regions with strong optical turbulence through the use of effective beam parameters [14]-[15]. Following [11], we will define $\Lambda_0$ and $\Theta_0$ as the input plane beam parameters that relate to the beam radius and phase front radius of curvature through

$$\Lambda_0 = \frac{2L}{kW_0^2}, \quad \Theta_0 = 1 - \frac{L}{F_0},$$
(2.31)

Subsequently, we are able to define output plane beam parameters

$$\Lambda = \frac{\Lambda_0}{\Lambda_0^2 + \Theta_0^2}, \quad \Theta = \frac{\Theta_0}{\Lambda_0^2 + \Theta_0^2},$$
(2.32)

that will allow us to simplify the mathematical expressions for the random phase correlations for different sources. We can see here that for the particular cases of $\Lambda_0 = 0, \Theta_0 = 1$ we have a plane wave, and $\Lambda_0 = 0$, $\Theta_0 = 0$ gives us a spherical wave.

The method of effective beam parameters maybe used to extend these following formulas into the strong regime by replacing $\Lambda$ and $\Theta$ by their effective beam parameters [11]

$$\Lambda_e = \frac{\Lambda}{1 + 4q\Lambda/3}, \quad \Theta_e = \frac{\Theta - 2q\Lambda/3}{1 + 4q\Lambda/3}.$$
(2.33)

# Chapter 3

# Laser Beam Propagation Through Oceanic Turbulence

## 3.1 Scintillation Index

We begin our investigation by determining the fourth-order statistics of a propagating beam and in particular the scintillation index, or normalized variance of the fluctuating intensity . The scintillation index is crucial in many applications such as communication links and laser radar and will be an important part of understanding oceanic turbulence. As mentioned in section 2.3, we choose to study the scintillation properties first as it will enable us to categorize the turbulence as being in either the weak or strong regime. This determination will affect the way we calculate the other properties of the beam as we go forward and will necessitate the use of the method of effective beam parameters.

In this chapter we begin by considering a scalar beam-like field $U(\boldsymbol{\rho}, 0)$ propagating in a linear random medium at a point with the position vector $\mathbf{r} = (x, y)$ and propagation distance $z$, from the source plane $z = 0$ into the half-space $z > 0$. Assuming the beam is generated by the lowest order Gaussian source of unit amplitude:

$$z = 0; \quad U_0(\boldsymbol{\rho}, 0) = \exp(-\frac{\rho^2}{W_0^2} - \frac{ik\rho^2}{2F_0}), \tag{3.1}$$

where $W_0$ and $F_0$ are the beam radius and phase front radius of curvature and $k$ is the wave number. At this point, having specified explicitly our source we can calculate the correlation function of the complex phase as in equation 2.8 for this particular case of a scalar Gaussian beam. For beam, it has been shown that we can write the complex phase correlations as [11]

$$\langle \exp[\psi^*(\mathbf{r}_1, \boldsymbol{\rho}_1, L) + \psi(\mathbf{r}_1, \boldsymbol{\rho}_2, L)]\rangle_m$$
$$= \exp[2E_1(0,0) + E_2(\mathbf{r}_1, \mathbf{r}_2)], \tag{3.2}$$

where we have for a Gaussian beam

$$E_1(0,0) = -2\pi^2 k^2 L \int_0^\infty \kappa \Phi_n(\kappa) d\kappa, \tag{3.3}$$

and

$$E_2(\mathbf{r}_1, \mathbf{r}_2) = 4\pi^2 k^2 L \int_0^1 \int_0^\infty \kappa \Phi_n(\kappa) J_0\{\kappa([1 - \bar{\Theta}\xi]\mathbf{p} - 2i\Lambda\xi\mathbf{r})\} \exp[-\frac{\Lambda L \kappa^2 \xi^2}{k}] d\kappa d\xi. \tag{3.4}$$

Here $\mathbf{p} = \mathbf{r}_1 - \mathbf{r}_2$, $\mathbf{r} = (\mathbf{r}_1 + \mathbf{r}_2)/2$ are the sum and difference vectors, $L$ is the propagation distance, $\xi$ is a normalized distance variable $\xi = 1 - z/L$, and $J_0$ is the zero order Bessel Function. $\Phi_n$ represents the power spectrum of the turbulence, and $\bar{\Theta} = 1 - \Theta$. We also recall that $\Lambda$ and $\Theta$ are the output plane beam parameters

given in equation 2.32. This gives us a final expression for the cross spectral density

$$W_2(\mathbf{r}_1, \mathbf{r}_2, L) = \langle U^*(\mathbf{r}_1, L)U(\mathbf{r}_2, L)\rangle$$

$$= \iint U^*(\boldsymbol{\rho}_1, 0)U(\boldsymbol{\rho}_2, 0)(\frac{k}{2\pi L})^2 \exp[-ik\frac{(\mathbf{r}_1 - \boldsymbol{\rho}_1)^2 - (\mathbf{r}_2 - \boldsymbol{\rho}_2)^2}{2L}] \tag{3.5}$$

$$\times \exp[2E_1(0,0) + E_2(\mathbf{r}_1, \mathbf{r}_2)]d^2\rho_1 d^2\rho_2.$$

We will also need to calculate the fourth order coherence function defined in equation 2.12 for the specific case of the scalar Gaussian beam. It has been shown that we can write this as [11]

$$W_4(\mathbf{r}_1, \mathbf{r}_2, \mathbf{r}_3, \mathbf{r}_4, L) = U_0(\mathbf{r}_1, L)U_0^*(\mathbf{r}_2, L)U_0(\mathbf{r}_3, L)U_0^*(\mathbf{r}_4, L)$$

$$\times \langle \exp[\psi(\mathbf{r}_1, L) + \psi^*(\mathbf{r}_2, L) + \psi(\mathbf{r}_3, L) + \psi^*(\mathbf{r}_4, L)]\rangle \tag{3.6}$$

$$= W_2(\mathbf{r}_1, \mathbf{r}_2, L)W_2(\mathbf{r}_3, \mathbf{r}_4, L) \exp[E_2(\mathbf{r}_1, \mathbf{r}_4) + E_2^*(\mathbf{r}_3, \mathbf{r}_2)$$

$$+ E_3(\mathbf{r}_1, \mathbf{r}_3) + E_3^*(\mathbf{r}_2, \mathbf{r}_4)].$$

Here we add another equation given by [11]

$$E_3(\mathbf{r}_1, \mathbf{r}_2) = -4\pi^2 k^2 L \int_0^1 \int_0^\infty \kappa \Phi_n(\kappa) J_0[(1 - \bar{\Theta}\xi - i\Lambda\xi)\kappa|\mathbf{p}|] \tag{3.7}$$

$$\times \exp[-\frac{\Lambda L\kappa^2\xi^2}{k}] \exp[-\frac{iL\kappa^2}{k}\xi(1 - \bar{\Theta}\xi)]d\kappa d\xi.$$

Recall that we define the scintillation index as

$$\sigma_I^2(\mathbf{r}, L) = \frac{\langle I^2(\mathbf{r}, L)\rangle - \langle I(\mathbf{r}, L)\rangle^2}{\langle I(\mathbf{r}, L)\rangle^2}, \tag{3.8}$$

with $I(\mathbf{r}, L)$ given by equation 2.10 and $\langle I^2(\mathbf{r}, L)\rangle$ given by equation 2.15. We are

now able to calculate the correlation of the complex phase in the fourth order for the specific case of the Gaussian beam, yielding

$$\langle I^2(\mathbf{r}, L)\rangle = W_4(\mathbf{r}, \mathbf{r}, \mathbf{r}, \mathbf{r}, L)$$

$$= \langle I(\mathbf{r}, L)\rangle^2 \exp(2 \text{ Re } [E_2(\mathbf{r}, \mathbf{r}) + E_3(\mathbf{r}, \mathbf{r})]). \tag{3.9}$$

By inserting equations 3.4 and 3.7 into equation 3.9 and subsequently into equation 3.8, we find that the scintillation index of a Gaussian beam can be represented by its longitudinal, or on-axis component, $\sigma_{I,l}^2(0, L)$ and radial component $\sigma_{I,r}^2(\mathbf{r}, L)$ [11], i.e.

$$\sigma_I^2(\mathbf{r}, L) = \sigma_{I,l}^2(0, L) + \sigma_{I,r}^2(\mathbf{r}, L), \tag{3.10}$$

where

$$\sigma_{I,l}^2(0, L) = 8\pi^2 k^2 L \int\limits_0^1 \int\limits_0^\infty \kappa \Phi_n(\kappa) \exp\left[-\frac{\Lambda L \kappa^2 \xi^2}{k}\right]$$

$$\times \left\{1 - \cos\left[\frac{L\kappa^2}{k}\xi(1 - (1 - \Theta)\xi)\right]\right\} d\kappa d\xi, \tag{3.11}$$

and

$$\sigma_{I,r}^2(\mathbf{r}, L) = 8\pi^2 k^2 L \int\limits_0^1 \int\limits_0^\infty \kappa \Phi_n(\kappa) \exp\left[-\frac{\Lambda L \kappa^2 \xi^2}{k}\right]$$

$$\times [I_0(2\Lambda r \xi \kappa) - 1] \, d\kappa d\xi, \; r = |\mathbf{r}|. \tag{3.12}$$

Here $I_0(x)$ is the modified Bessel function of order zero and with $\Lambda$ and $\Theta$ given by equations 2.31 and 2.33. We are now able to substitute the oceanic turbulence

spectrum, equation 1.6, directly into equations 3.11 and 3.12 to calculate the scintillation of propagating beams.

We will start by investigating the scintillation index of a plane wave, known as the Rytov variance [11], which we will use to distinguish the strong and weak turbulence regimes, as well as the case of a spherical wave. For this we will chose $\Lambda = 0, \Theta = 1$ for the case of a plane wave, and $\Lambda = 0, \Theta = 0$ for the case of the spherical wave. In these two specific cases the radial component of the scintillation index, equation 3.12, vanishes. Due to the sensitivity of the numerical integration including the limit used to approach the $+\infty$ upper bound on the integral in equation 3.11, some reproductions of these results may differ slightly from those presented here. This can change slightly the affect that propagation distance has on the separation between weak and strong turbulence regimes.

Figure 3.1 plots the scintillation index of both a plane wave and spherical wave as a function of propagation distance for several values of $\chi_T$, the rate of mean-squared temperature variance dissipation [17]. The difference in absolute scintillation between the plane and spherical waves is approximately one order of magnitude. This is a much larger difference than what we find for the traditional Kolmogorov spectrum of atmospheric turbulence which gives a ratio of approximately 0.4 [11]. Drawn on Figure 3.1(A) is a line marking the separation between regions of weak and strong turbulence. Traditionally in atmospheric turbulence the Rytov variance, or scintillation index of a plane wave, is used as the threshold where $\sigma_R^2 << 1$ is said to be weak turbulence and $\sigma_R^2 >> 1$ is the strong regime. We see that the onset of this strong turbulence regime begins as soon as about 10m and as late as perhaps 100 meters with certain values
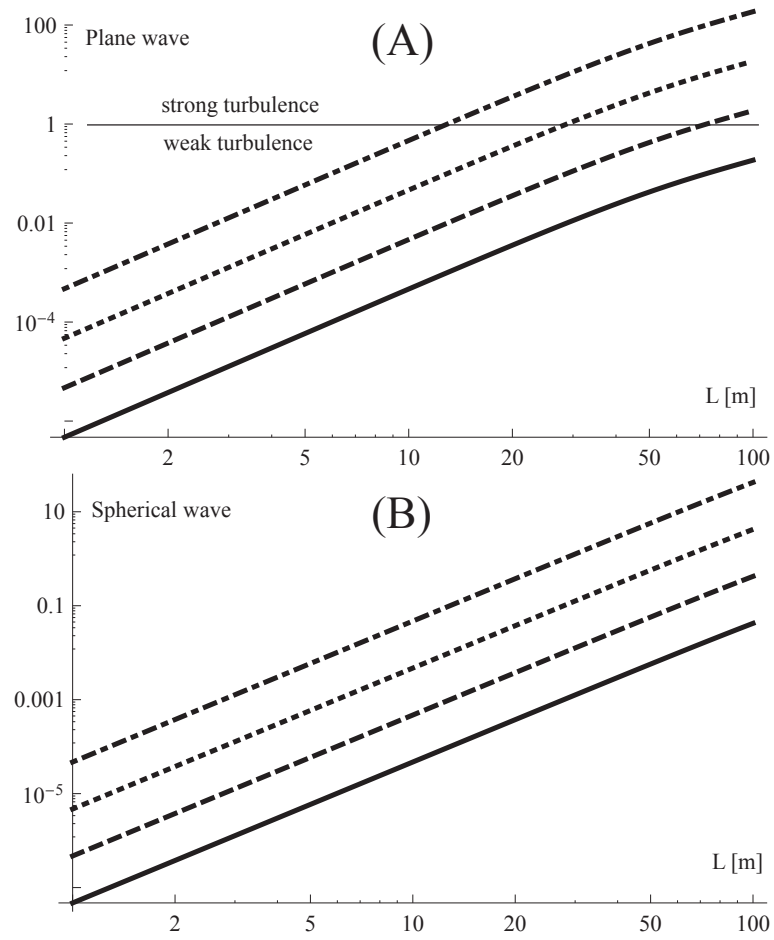
Figure 3.1: The scintillation index of (A) plane wave and (B) spherical wave vs. propagation distance $L$ [m] for several values of $\chi_T$: $\chi_T = 10^{-8}$ $K^2/s$ (solid curve), $\chi_T = 10^{-7}$ $K^2/s$ (dashed curve), $\chi_T = 10^{-6}$ $K^2/s$ (dotted curve), $\chi_T = 10^{-5}$ $K^2/s$ (dash-dotted curve). $\omega = -2.5$, $\varepsilon = 10^{-5}$ $m^2/s^3$. From Ref. [17]
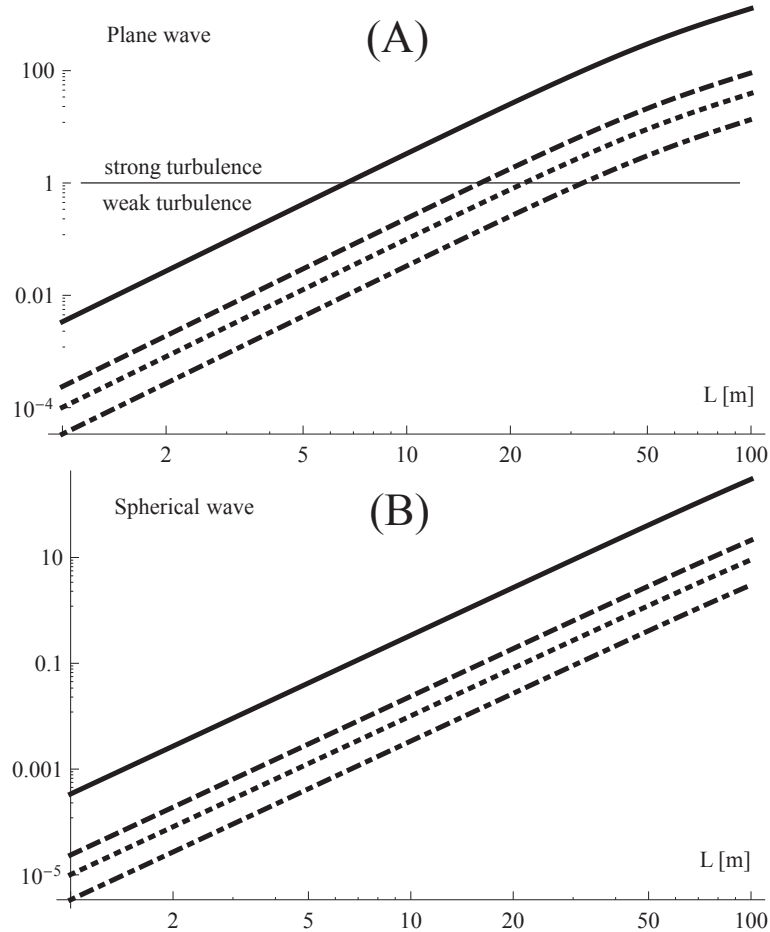
Figure 3.2: The scintillation index of (A) plane wave and (B) spherical wave vs. propagation distance $L$ [m] for several values of $\omega$: $\omega = -0.1$ (solid curve); $\omega = -0.5$ (dashed curve); $\omega = -1$ (dotted curve), $\omega = -4.9$ (dash-dotted curve). $\chi_T = 10^{-6}$ $K^2/s$, $\varepsilon = 10^{-5}$ $m^2/s^3$. From Ref. [17]

of $\chi_T$. Dependence on the parameter $\varepsilon$ is not plotted as it is evident from equation 1.6 that it is monotonic and inverse to that of $\chi_T$. Figure 3.2 shows the dependence of plane and spherical wave scintillation on the parameter $w$. We see clearly that for values closer to $w = 0$, that is heavier salinity dominated fluctuations, we have a higher scintillation than for temperature dominant fluctuations with values closer to $w = -5$.

Figure 3.3 plots the ratio of the scintillation index of a spherical wave to that
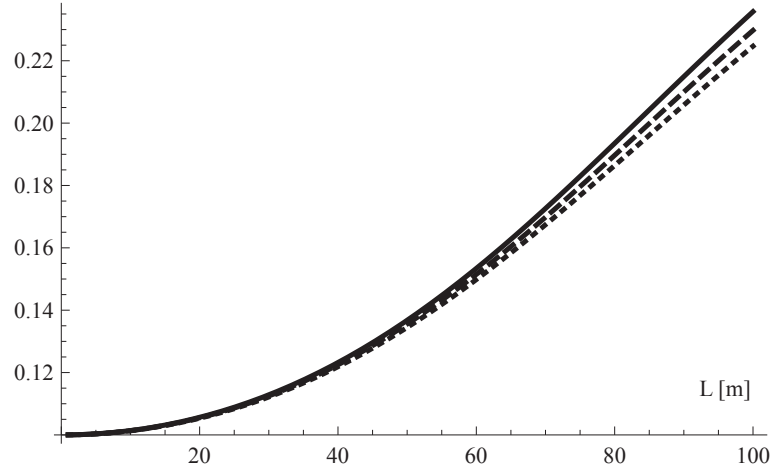
Figure 3.3: The ratio of the scintillation indexes of a spherical to a plane waves vs. propagation distance $L$ [m] for several values of $\omega$: $\omega = -0.1$ (solid curve), $\omega = -1$ (dashed curve), $\omega = -4.9$ (dotted curve). $\chi_T = 10^{-6}\ K^2/s$, $\varepsilon = 10^{-5}\ m^2/s^3$. From Ref. [17]

of a plane wave vs. propagation distance [17]. In this figure we can see that the ratio starts at roughly 0.1 and grows with propagation distance, which is in contrast to atmospheric turbulence with the Kolmogorov spectrum where it is approximately constant at 0.4. This ratio is independent of $\chi_T$ and $\varepsilon$ but does vary slightly with $w$ as seen from the three separate curves.

Figure 3.4 [17] shows the scintillation index of a Gaussian beam normalized by that of a plane wave. It is plotted as a function of $\Lambda_0$, the initial width of the beam normalized by the first Fresnel zone defined in equation 2.31. Functionally, this represents the near field when $\Lambda_0 << 1$ and the far field when $\Lambda_0 >> 1$. This normalized value of scintillation does not depend on $\chi_T$ or $\varepsilon$. The impact of the parameter $w$ is shown in the plot. For on-axis scintillation $w$ does not impact the normalized scintillation appreciably but does have noticeable impact on the values on the beam edge, that is the point where $r = (\Lambda^2 + \Theta^2)^{1/2}$. For $\Lambda_0 = 1$ the ratio
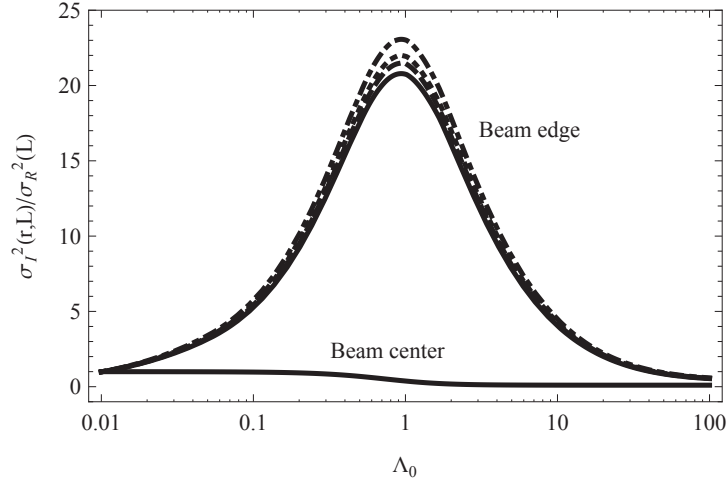
Figure 3.4: Scintillation index of a collimated Gaussian beam normalized by the scintillation index of the plane wave at $r = 0$ and $r = W$, the parameters are the same as in Fig. 3.2. From Ref. [17]

can be larger than 20, which is considerably larger than that found typically in the atmospheric case where the ratio tends to be approximately 4-5.

## 3.2  Average Intensity Characteristics

Given what we know now about the scintillation and the very early onset of the strong turbulence regime, we can proceed to calculate the second order statistics, including the intensity profile, using the method of effective beam parameters outlined in Chapter 2.3. Recall that the intensity at a propagation distance $L$ and point in the x-y plane $\mathbf{r}$ is defined as

$$I(\mathbf{r}, L) = W_2(\mathbf{r}, \mathbf{r}, L). \tag{3.13}$$

By substituting the oceanic turbulence spectrum, equation 1.6, directly into equations 3.3 and 3.4, and finally into equation 3.5 we can directly calculate the intensity profile. In the following figures $\chi_T = 10^{-7} \frac{m^2}{s^3}$, $\varepsilon = 10^{-5} \frac{K^2}{s}$, $\lambda = 0.417 \times 10^{-6}m$, initial beam size $W_0 = 0.01m$, and $F_0 = \infty$ unless specified otherwise.

Figure 3.5 shows the intensity profiles of a Gaussian beam propagating through several different distances of oceanic turbulence with several different values of $w$, the parameter relating the relative contributions of temperature and salinity to the turbulence [18]. These plots show that with a value of $w$ closer to 0, the upper limit representing the case where salinity fluctuations are dominant, the intensity is degraded much faster than for values approaching the lower bound of $w = -5$, the case when temperature fluctuations are more prominent.

In these plots recall that we have only taken into account the influence of optical turbulence on the beam, and not absorption. For the wavelength chosen, $0.417 \times 10^{-6}$m, the absorption coefficient of pure water has been found to be $a_w = 0.00441m^{-1}$ [16]. Using this we can calculate the drop in intensity due to absorption using the well known Beer's Law formula

$$I(\mathbf{r}, L) = I_0(\boldsymbol{\rho}, 0) \exp[-a_w L]. \tag{3.14}$$

At propagation distances of $L$ equal to 10, 30, and 70 meters this leaves 95.66%, 87.55%, and 73.34% of the original intensity. If we compare these results with the figures, we can see that the on-axis intensity change due to optical turbulence alone can be significant and in some cases larger than that of absorption. Salinity
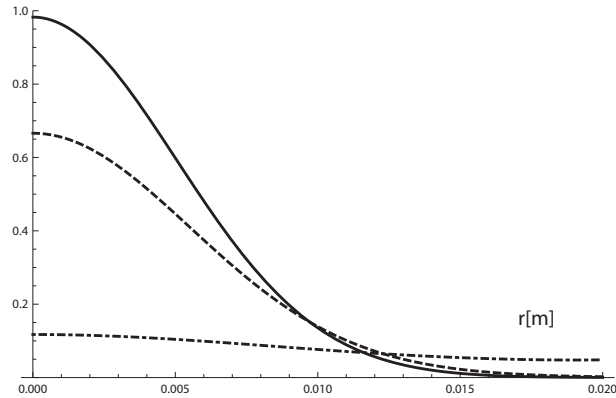
(a) $w = -0.2$
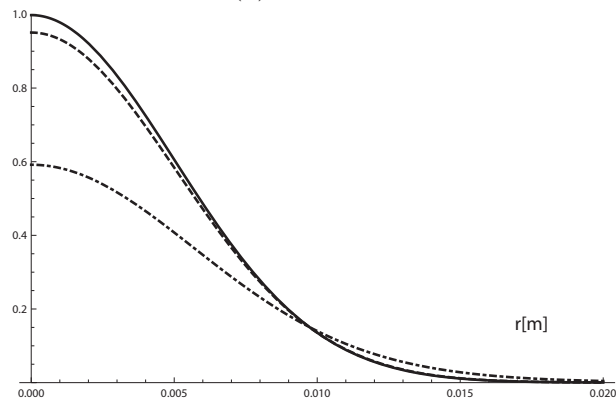


(b) $w = -1$
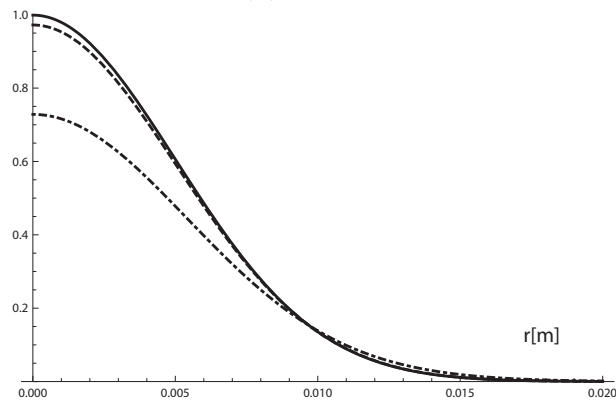


(c) $w = -2$

Figure 3.5: Intensity profiles of a Gaussian beam as a function of radial distance from the beam axis for different propagation lengths and $w$ values. All plots have $\chi_T = 10^{-7} \frac{m^2}{s^3}$, $\varepsilon = 10^{-5} \frac{K^2}{s}$, $L = 10m$ (solid curve), $L = 30m$ (dashed curve), and $L = 70m$ (dot-dashed curve). From Ref. [18]
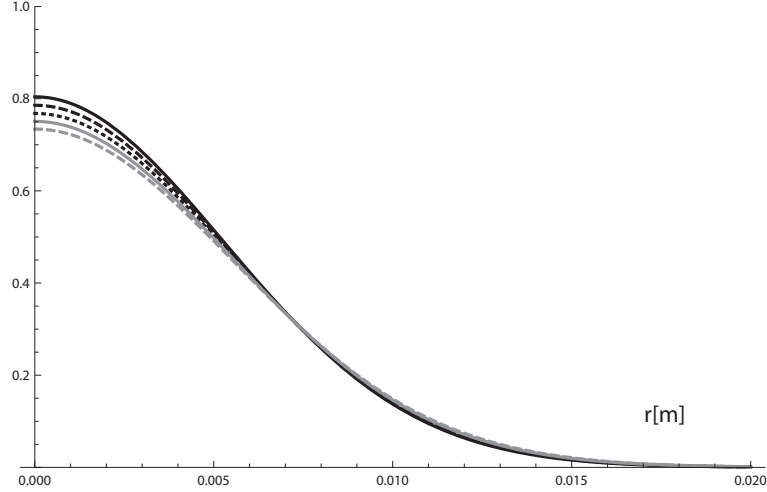
Figure 3.6: Intensity distribution vs. radial distance from the beam axis for several different wavelengths with $w = -1$. $\lambda = 400nm$ (solid black curve), $\lambda = 500nm$ (dashed black curve), $\lambda = 600nm$ (dot-dashed black curve), $\lambda = 700nm$ (solid gray curve), $\lambda = 800nm$ (dashed gray curve). From Ref. [18]

dominated fluctuations can result in much more beam degradation than that due to the absorption from pure water.

Figure 3.6 examines the dependence of the intensity distribution on the wavelength of the source beam at a propagation distance of 50 meters. We see that across the visible spectrum, from 400nm to 800nm, higher wavelengths are affected more by the turbulence, if only slightly.

## 3.3 Coherence Properties

Along with intensity we can investigate the coherence properties of propagating beams using the second order cross spectral density $W_2$, given by equation 3.5. Again we recall that the degree of coherence is given by the formula [11]

$$\mu(\mathbf{r}_1, \mathbf{r}_2, z) = \frac{W_2(\mathbf{r}_1, \mathbf{r}_2, z)}{\sqrt{W_2(\mathbf{r}_1, \mathbf{r}_1, z)W_2(\mathbf{r}_2, \mathbf{r}_2, z)}} = \frac{W_2(\mathbf{r}_1, \mathbf{r}_2, z)}{\sqrt{I(\mathbf{r_1}, z)I(\mathbf{r_2}, z)}}. \tag{3.15}$$

In this study we will choose points $\mathbf{r}_1$ and $\mathbf{r}_2$ that are directly opposite each other with respect to the beam axis for all calculations. Figure 3.7 shows the degree of coherence profile of Gaussian beams under several different values of the turbulence parameter $w$ and several propagation distances [18]. Highlighted in the subplot of Figure 3.7a we can see that the coherence profile becomes wider at 70m that it is at 30m. This property of the beam is consistent with results for atmospheric turbulence [11] and can be seen more clearly in Figure 3.8a. This figure fixes the parameter $w = -0.2$ and plots the coherence radius, that is the $1/e$ point of the degree of coherence as a function of propagation distance for a plane wave, spherical wave, and Gaussian beam. The increase in coherence radius at further propagation distances can be seen for the Gaussian beam (dashed plot), agreeing with Figure 3.7a. These plots begin at a 10m propagation distance due to shorter distances being more computationally intensive and not offering any additional value.

Figure 3.8b shows the coherence radii of a spherical wave and a Gaussian beam normalized by that of a plane wave and is readily compared to the atmospheric case shown in Figures 7.2 and 7.4 in [11]. While the ratio of spherical to plane waves stays rather consistent, with only a small downward slope, the ratio for the Gaussian beam starts at 1:1 but then saturates at large propagation distances to that of the spherical wave. We have used a smaller value of $w$, here $w = -0.2$, to exaggerate this effect due to the smaller value causing stronger turbulence.
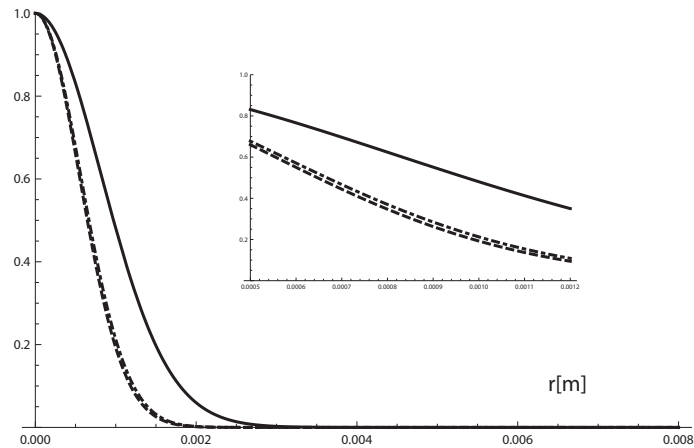
(a) $w = -0.2$
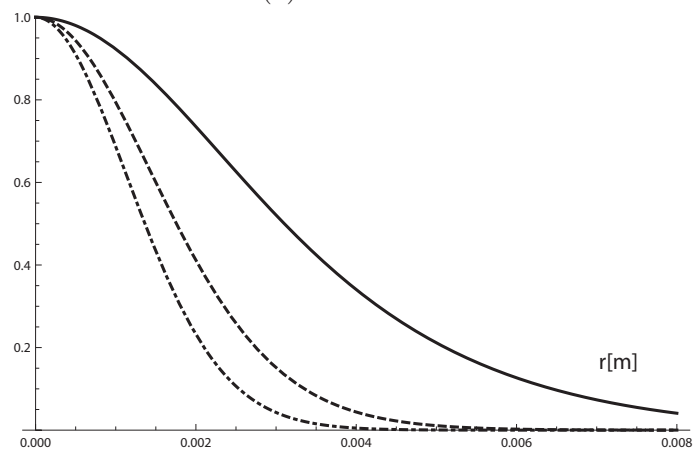
(b) $w = -1$
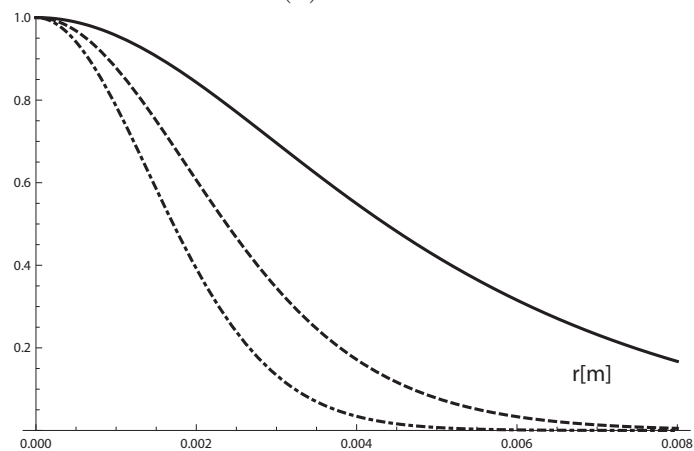
(c) $w = -2$

Figure 3.7: Degree of coherence profiles of a Gaussian beam as a function of separation distance for different propagation lengths and $w$ values. All plots have $\chi_T = 10^{-7} \frac{m^2}{s^3}$, $\varepsilon = 10^{-5} \frac{K^2}{s}$, $L = 10m$ (solid curve), $L = 30m$ (dashed curve), and $L = 70m$ (dot-dashed curve). From Ref. [18]
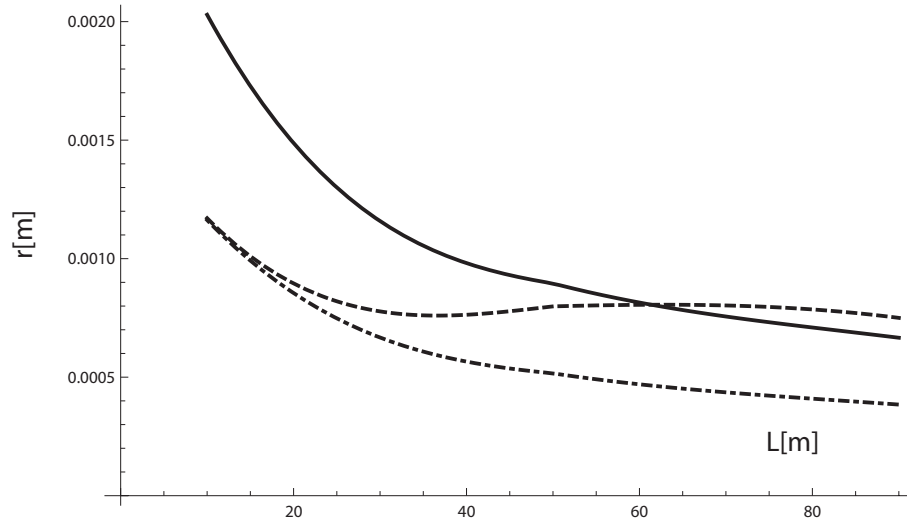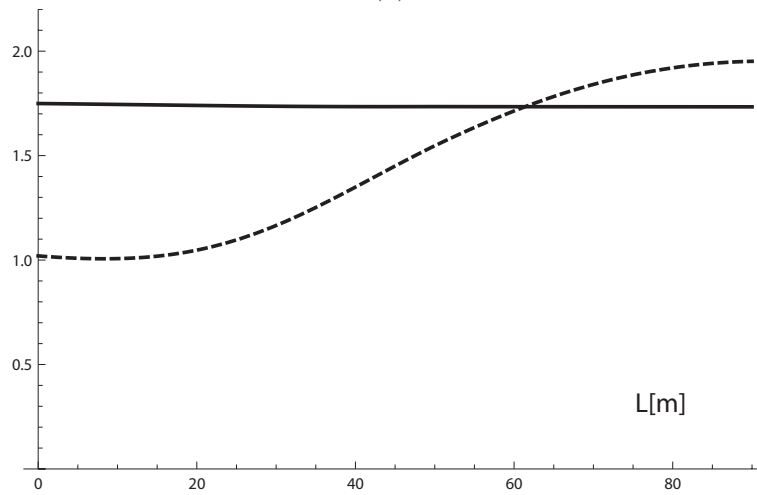
Figure 3.8: (A) The coherence radius of a plane wave (dot-dashed curve), spherical wave (solid curve) and Gaussian beam (dashed curve) as a function of propagation length. (B) The coherence radius of a spherical wave (solid curve) and Gaussian beam (dashed curve) normalized by that of a plane wave as a function of propagation length. Both plots shown take $w = -0.2$ From Ref. [18]

# Chapter 4

# Spectral Changes in Stochastic Light Beams in Oceanic Turbulence

Often times when measuring the spectrum of light from a distant source, it is taken for granted that the normalized spectral distribution at the detector is the same as that of the source. It has been shown that this is not true for all sources, and in fact the spectrum of light can change even upon propagation in a vacuum [37]. For this spectral shift to occur we must insure that the source generates a highly directional, partially coherent beam with a narrow initial spectrum. Sources such as unbounded sun light or a monochromatic laser beam would not allow this shift to occur. In addition to these changes occurring in a vacuum, it has been seen that the spectrum of partially coherent beams can exhibit even more complex behavior when propagating through random media, such as atmospheric turbulence or human tissue ([38], [39],[40]). This topic is critical as the spectral composition of beams can be used as a carrier of information in communications or remote sensing ([41],[42]) and it has been shown that it can often times be helpful to use a partially coherent beam rather than deterministic when working in a random media ([43], [44]). If we intend to study beam propagation through oceanic turbulence we must take this spectral shift into account, particularly due to the varying absorption rates for different wavelengths of light in the ocean [16].

## 4.1 Spectral Properties

We will begin this study with an scalar Gaussian Schell-Model (GSM) beam with an explicit dependence on wavelength in the source plane given by

$$W_{2,0}(\boldsymbol{\rho}_1, \boldsymbol{\rho}_2; \lambda) = \mathcal{I}_0(\lambda) \exp\left[-\frac{(\boldsymbol{\rho}_1)^2 + (\boldsymbol{\rho}_2)^2}{4\sigma^2}\right] \exp\left[-\frac{(\boldsymbol{\rho}_1 - \boldsymbol{\rho}_2)^2}{2\delta^2}\right], \qquad (4.1)$$

previously described in Chapter 2.3.

Beginning with this source plane cross spectral density, we can insert it into equation 2.28 to calculate the result in the observation plane. For this we will need to explicitly calculate the propagator $K$ defined in equation 2.8 for the case of the scalar GSM beam. Following [11] we see that we can express the correlation of the complex phase as

$$\langle \exp[\psi^*(\boldsymbol{\rho}_1, \boldsymbol{r}_1) + \psi(\boldsymbol{\rho}_2, \boldsymbol{r}_2)]\rangle_m =$$

$$\exp\left[-4\pi^2 k^2 z \int\limits_0^1 \int\limits_0^\infty \kappa\Phi_n(\kappa)[1 - J_0[|(1-\xi)(\mathbf{r}_1 - \mathbf{r}_2) + \xi(\boldsymbol{\rho}_1 - \boldsymbol{\rho}_2)|\kappa]]d\kappa d\xi\right], \qquad (4.2)$$

Recalling that $J_0$ is the $0^{th}$ order Bessel function, if the fluctuations in the source are much stronger than those in the random medium, it is possible to approximate the Bessel function by its first two terms, i.e. $J_0(x) \approx 1 - \frac{1}{4}x^2$ and we can then write the propagator K as ( [20] - [22] )

$$K(\mathbf{r}_1, \mathbf{r}_2; \boldsymbol{\rho}_1, \boldsymbol{\rho}_2; z, \lambda) = \left(\frac{k}{2\pi z}\right)^2 \exp\left[-ik\frac{(\mathbf{r}_1 - \boldsymbol{\rho}_1)^2 - (\mathbf{r}_2 - \boldsymbol{\rho}_2)^2}{2z}\right]$$

$$\times \exp\left[-\frac{\pi^2 k^2 z}{3}[(\mathbf{r}_1 - \mathbf{r}_2)^2 + (\mathbf{r}_1 - \mathbf{r}_2)(\boldsymbol{\rho}_1 - \boldsymbol{\rho}_2) + (\boldsymbol{\rho}_1 - \boldsymbol{\rho}_2)^2]\int_0^\infty \kappa^3 \Phi_n(\kappa)d\kappa\right]. \quad (4.3)$$

From here we can directly insert equation 4.3 into equation 2.28 to find ([22] ,

$$W_2(\mathbf{r}_1, \mathbf{r}_2; z, \lambda) = \frac{\mathcal{I}_0(\lambda)}{\Delta^2(z)} \exp\left(-\frac{(\mathbf{r}_1 + \mathbf{r}_2)^2}{8\sigma^2 \Delta^2(z)}\right)$$

$$\times \exp\left(-\left[\frac{1}{2\Delta^2(z)}\left(\frac{1}{4\sigma^2} + \frac{1}{\delta^2}\right) + M(1 + \sigma^2) - \frac{M^2 z^2 \lambda^2}{8\pi^2 \sigma^2 \Delta^2(z)}\right](\mathbf{r}_1 + \mathbf{r}_2)^2\right) \quad (4.4)$$

$$\times \exp\left(\frac{i\pi(\mathbf{r}_2^2 - \mathbf{r}_1^2)}{\lambda R(z)}\right),$$

with

$$\Delta^2(z) = 1 + \left(\frac{z\lambda}{2\pi\sigma}\right)^2\left(\frac{1}{4\sigma^2} + \frac{1}{\delta^2}\right) + \frac{M z^2 \lambda^2}{2\pi^2 \sigma^2},$$

$$M = \frac{4\pi^4 z}{3\lambda^2}\int_0^\infty \kappa^3 \Phi_n(\kappa)\,d\kappa, \quad R(z) = \frac{4\pi^2 \sigma^2 \Delta^2(z) z}{4\pi^2 \sigma^2 \Delta^2(z) + M z^2 \lambda^2 - 4\pi^2 \sigma^2}. \quad (4.5)$$

It then follows that the wavelength dependent intensity, evaluated as in equation 2.10 can be expressed as

$$I(\mathbf{r}, \lambda) = \frac{\mathcal{I}_0(\lambda)}{\Delta^2(z)} \exp\left[-\frac{\mathbf{r}^2}{2\sigma^2 \Delta^2(z)}\right]. \quad (4.6)$$

For the analysis here it will be of interest to evaluate the normalized intensity given by [29]

$$I_N(\mathbf{r}; \lambda) = I(\mathbf{r}; \lambda)/\int_0^\infty I(\mathbf{r}; \lambda)\,d\lambda, \quad (4.7)$$

Further, we will be interested in the new central frequency of the beam found with [38]

$$\lambda_1(\mathbf{r}) = \int_0^\infty \lambda I(\mathbf{r}; \lambda)\,d\lambda/\int_0^\infty I(\mathbf{r}; \lambda)\,d\lambda. \quad (4.8)$$

Using this new central frequency, we can establish a normalized spectral shift

$$\varrho(\mathbf{r}) = \frac{\lambda_1(\mathbf{r}) - \lambda_0}{\lambda_0}, \tag{4.9}$$

which shows a blue shift when $\varrho$ takes negative values, and a red shift for positive values. In the figures that follow, $\lambda_0 = 0.5435 \times 10^{-6}\ m$, $\Pi = \lambda_0/6$; $\sigma = 0.01\ m$; $\delta = 0.0001\ m$.

## 4.2  Numerical Results

Figures 4.1 and 4.2 show density plots of the actual spectral shift overlapped with contour plots of the normalized spectral shift of a beam on propagation [45]. Figure 4.1 and its four subplots show the dependence of both the position of a point relative to the center of the beam, (on the y-axis), and that of varying the value of $\chi_T$. The four plots have values of (a) $\chi_T = 10^{-10}\ K^2/s$, corresponding to very weak turbulence, (b) $\chi_T = 10^{-5}\ K^2/s$, (c) $\chi_T = 10^{-4}\ K^2/s$, and (d) $\chi_T = 10^{-2}\ K^2/s$, corresponding to very strong turbulence. We see in Figure 4.1a that for the case of very weak turbulence, the beam undergoes a blue shift after propagation while in the plots highlighting stronger turbulence, this shift is suppressed, and indeed ends up reconstructing its original spectrum. In the case with the strongest turbulence, the turbulence serves to suppress any source induced spectral changes almost completely, and the very minor change that does occur happens very near the source, on the order of 10 meters.
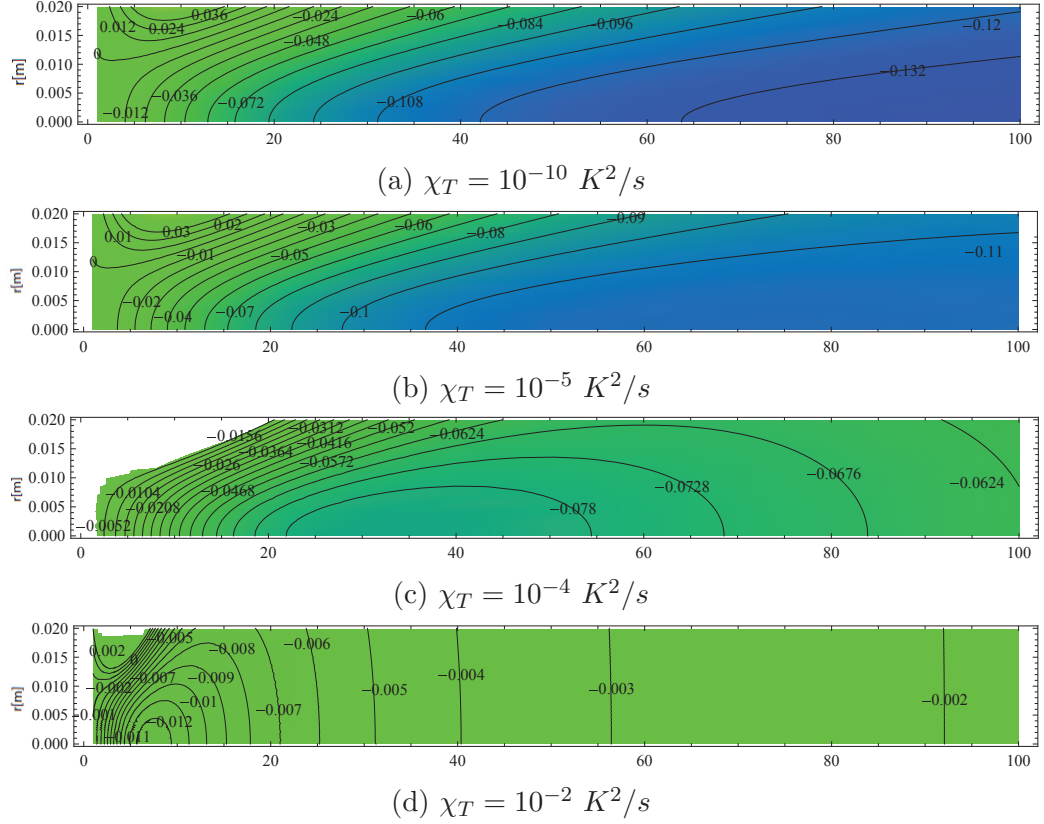
Figure 4.1: Density plots of actual spectral shift $\lambda_1$ overlapped with contour plots of normalized spectral shift $\varrho = \frac{\lambda_1 - \lambda_0}{\lambda_0}$ as a function of $z$ (horizontal axis, in meters) and $r$ (vertical axis, in meters) for (a) $\chi_T = 10^{-10}$ $K^2/s$; (b) $\chi_T = 10^{-5}$ $K^2/s$, (c) $\chi_T = 10^{-4}$ $K^2/s$; (d) $\chi_T = 10^{-2}$ $K^2/s$; $\varepsilon = 10^{-4}$ $m^2/s^3$, $w = -4.5$. From Ref. [45]

Figure 4.2 highlights the on-axis impact of the three major parameters of oceanic turbulence, (a) rate of dissipation of mean-square temperature $\chi_T$; (b) density gradient ratio $w$ and (c) energy dissipation rate $\varepsilon$. Figure 4.2a shows that for values of $\chi_T$ higher than $10^{-5}$ reconstruction of the initial spectrum can occur. At this point the turbulence is strong enough to suppress the source correlation induced spectral changes. Figure 4.2b shows a similar property pertaining to the density gradient ratio parameter $w$, that is, we must have a value very close to 0, indicating salinity dominant fluctuations and thus stronger turbulence, in order to suppress the changes. Figure 4.2c shows the effect of $\epsilon$ which follows similarly to $\chi_T$ albeit in an inverse manner and without as significant an effect.
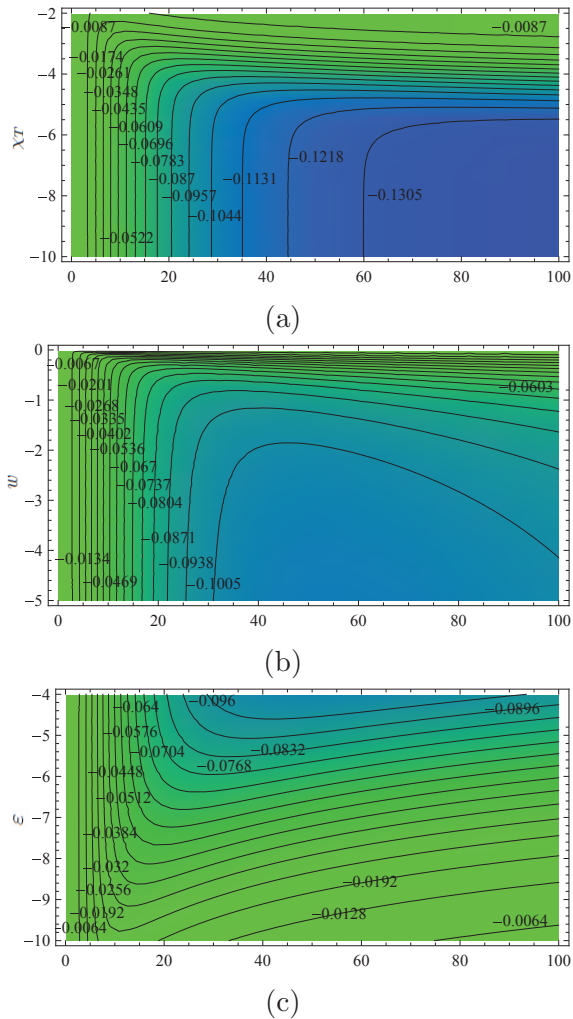
Figure 4.2: Density plots of actual spectral shift $\lambda_1$ overlapped with contour plots of normalized spectral shift $\varrho = \frac{\lambda_1 - \lambda_0}{\lambda_0}$ as a function of $z$ (horizontal axis, in meters) and (a) $\chi_T$, on a log scale for $\varepsilon = 10^{-4}\ m^2/s^3$, $w = -2.5$, (b) $w$ for $\varepsilon = 10^{-4}\ m^2/s^3$, $\chi_T = 10^{-4.5}\ K^2/s$, (c) $\varepsilon$, on a log scale (vertical axis) for $\chi_T = 10^{-4.5}\ K^2/s$, $w = -2.5$; $r = 0$. From Ref. [45]

# Chapter 5

# Polarization Properties of Stochastic Beams in Oceanic Turbulence

## 5.1 Electromagnetic Stochastic Beam Propagation

We have so far been interested in only cases involving a scalar beam, but we will now switch to investigating the case of an electromagnetic beam. We start by introducing a beam with its source located in the plane $z = 0$ defined by $\mathbf{E}(\boldsymbol{\rho}, \lambda) = [E_x(\boldsymbol{\rho}, \lambda), E_y(\boldsymbol{\rho}, \lambda)]$ where $E_x$ and $E_y$ are the mutually orthogonal components of the electric field fluctuating with wavelength $\lambda$. Here $\boldsymbol{\rho}$ is again the two-dimensional vector $\boldsymbol{\rho} = (\rho_x, \rho_y)$ in the source plane. We can now describe the second-order correlation properties of this electromagnetic beam at two points, $\boldsymbol{\rho}_1$ and $\boldsymbol{\rho}_2$ using the cross-spectral density matrix defined by [19]

$$\mathbf{W} = [W_{ij}(\boldsymbol{\rho}_1, \boldsymbol{\rho}_2; \lambda)], \quad (i, j = x, y), \tag{5.1}$$

where

$$W_{ij,0}(\boldsymbol{\rho}_1, \boldsymbol{\rho}_2; \lambda) = \langle E_i^*(\boldsymbol{\rho}_1; \lambda) E_j(\boldsymbol{\rho}_2; \lambda) \rangle, \quad (i = x, y; j = x, y), \tag{5.2}$$

is the familiar scalar correlation function of the fields averaged over the ensemble of realizations.

Following the assumption that the fluctuations in the index of refraction are small in comparison to the wavelength of light, the components of the electric field $E_i$ at any point $\mathbf{r}$ satisfy the wave equations of the form

$$\nabla^2 E_i(\mathbf{r}, z, \lambda) + k^2 n^2(\mathbf{r}, z) E_i(\mathbf{r}, z, \lambda) = 0, \tag{5.3}$$

where $k = 2\pi/\lambda$ is the wave number of the light, and $i = x, y, z$. In this study, we will only be interested in beam like fields, and therefore can neglect the z-component. Additionally, any and all correlation between the x and y components of the electric field will occur through initial conditions in the source plane, and not upon propagation in the medium.

We recall from equation 2.29 that upon propagation we have,

$$W_{2,ij}(\mathbf{r}_1, \mathbf{r}_2; z, \lambda) = \int \int W_{ij,0}(\boldsymbol{\rho}_1, \boldsymbol{\rho}_2; \lambda) K(\mathbf{r}_1, \mathbf{r}_2; \boldsymbol{\rho}_1, \boldsymbol{\rho}_2; z, \lambda) d^2\rho_1 d^2\rho_2, \quad (i, j = x, y),$$
$$\tag{5.4}$$

with K the propagator now being defined by equation 4.3. For the following analysis of the polarization properties we will be investigating the electromagnetic Gaussian Schell Model (EMGSM) beam defined in Chapter 2.4 whose source was given as

$$W_{ij,0}(\boldsymbol{\rho}_1, \boldsymbol{\rho}_2, \lambda) = A_i A_j B_{ij} \exp\left[-\left(\frac{\boldsymbol{\rho}_1^2}{4\sigma_i^2} + \frac{\boldsymbol{\rho}_2^2}{4\sigma_j^2}\right)\right] \exp\left[-\frac{(\boldsymbol{\rho}_1 - \boldsymbol{\rho}_2)^2}{2\delta_{ij}^2}\right], \quad (i, j = x, y),$$
$$\tag{5.5}$$

## 5.2 Polarization Properties

The focus of this section will be on the evolution of the polarization properties of an EMGSM beam traveling through oceanic turbulence. In the interest of providing a complete view of the evolution of the beam, the change in spectral density of the beam will be shown along with the polarization characteristics. The spectral density of an electromagnetic stochastic beam is defined by the expression

$$S(\mathbf{r}; \lambda) = Tr[\mathbf{W}(\mathbf{r}, \mathbf{r}; \lambda)]. \tag{5.6}$$

The polarization of the beam can be characterized by the spectral degree of polarization which is defined by the formula [19]

$$P(\mathbf{r}; \lambda) = \sqrt{1 - \frac{4Det[\mathbf{W}(\mathbf{r}, \mathbf{r}; \lambda)]}{Tr[\mathbf{W}(\mathbf{r}, \mathbf{r}; \lambda)]^2}}, \tag{5.7}$$

and the spectral polarization ellipse defining the state of polarization of the fully polarized portion of the beam. In Eqs. 5.6 and 5.7 $Tr$ and $Det$ stand for trace and determinant of a matrix. Figure 5.1 shows the notation relevant to the polarization ellipse we will use in exploring the characteristics of the beam by expressing them as functions of $W$, the cross spectral density matrix [32]. The polarization angle, denoted $\psi$ gives the angle of the polarization and can be expressed by [19]

$$\psi(\mathbf{r}, \lambda) = \frac{1}{2} \left| \arctan \left( \frac{2Re[W_{xy}(\mathbf{r}, \mathbf{r}, \lambda)]}{W_{xx}(\mathbf{r}, \mathbf{r}, \lambda) - W_{yy}(\mathbf{r}, \mathbf{r}, \lambda)} \right) \right|. \tag{5.8}$$

The semi-axes of the ellipse will also be important in our analysis and can also be related to the cross-spectral density as follows,

$$\varsigma_{1,2}(\mathbf{r}, \lambda) = \frac{1}{\sqrt{2}} \left[ \sqrt{(W_{xx} - W_{yy})^2 + 4|W_{xy}|^2} \pm \sqrt{(W_{xx} - W_{yy})^2 + 4[ReW_{xy}]^2} \right]^{1/2}.$$

(5.9)

Here the $+$ and $-$ signs on the right side of the formula correspond to the major semi-axis $\varsigma_1$ and minor semi-axis $\varsigma_2$ of the ellipse, respectively. With these now fully defined, we can describe the ellipticity, or shape of the ellipse, by the ratio

$$\epsilon(\mathbf{r}, \lambda) = \frac{\varsigma_2(\mathbf{r}, \lambda)}{\varsigma_1(\mathbf{r}, \lambda)}.$$

(5.10)

When $\epsilon = 0$ the polarization state is linear, and for $\epsilon = 1$ the polarization state becomes circular. We are now able to describe the state of the beam as it propagates through oceanic turbulence fully. In the following results, unless specified to be otherwise, the parameters of both the beam source and oceanic turbulence are taken as $\lambda = 0.633\mu m$, $\sigma_x = \sigma_y = \sigma = 0.01m$, $\delta_{xx} = 0.0005$ m, $\delta_{yy} = 0.004$ m , $\delta_{xy} = 0.005$ m, $A_x = 1.3$, $A_y = 1$ and $B_{xy} = B_{yx} = 0.1$, $B_{xx} = B_{yy} = 1$, $\chi_T = 10^{-6}$, $\varepsilon = 10^{-7}$, $w = -2.5$

Figure 5.2 shows the typical evolution of the polarization ellipse upon propagation [33]. Each of the four plots, that show four different propagation distances, display the values of the spectral density, normalized by that at the source. It is apparent from these figures that the beams polarimetric properties change in a non-monotonic manner. We also see that at large propagation distances the polarization begins to
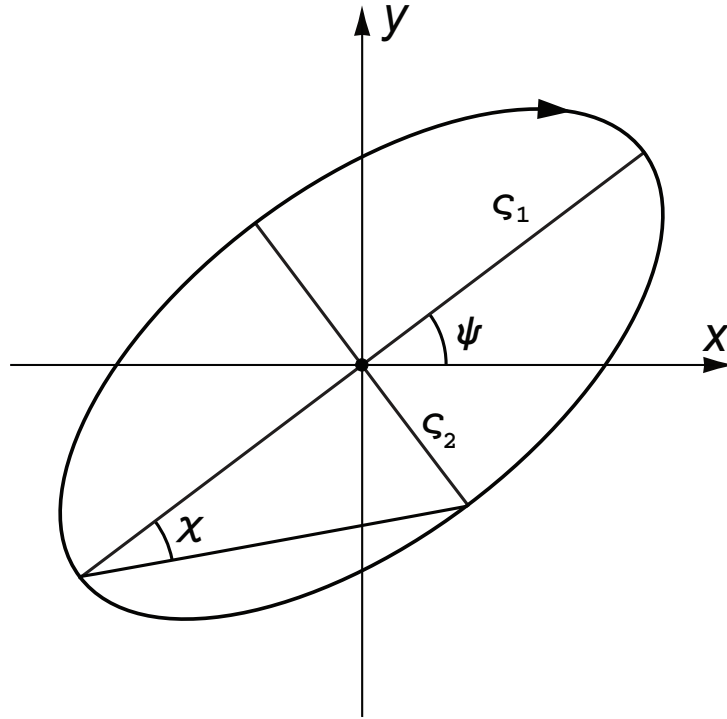
Figure 5.1: Notation relating to the parameters of polarization ellipse.

return to having the same properties as those at the source. This self reconstruction phenomenon is similar to that seen in atmospheric turbulence ([28], [34]), but different from that in human tissues ([35], [36]).

Figures 5.3 - 5.6 are all organized with the spectral density $S$ in plot (a), degree of polarization $P$ in plot (b), orientation angle $\psi$ in plot (c), and degree of ellipticity $\epsilon$ in plot (d), with the propagation distance $z$ on the horizontal axis, in meters. We start by looking at the dependence of the polarization properties on the beam source parameters. Figure 5.3 shows the dependence on $\delta_{xx}$, the source correlation property. The three curves represent $\delta_{xx} = 0.0005m$ (solid curves), $\delta_{xx} = 0.001m$ (dotted curves), $\delta_{xx} = 0.005m$ (dashed curves) while the two other r.m.s. correlation widths $\delta_{yy}$ and $\delta_{xy}$ are kept fixed. Here we see that while the spectral density is not affected largely by changes in the source correlation, the polarization properties
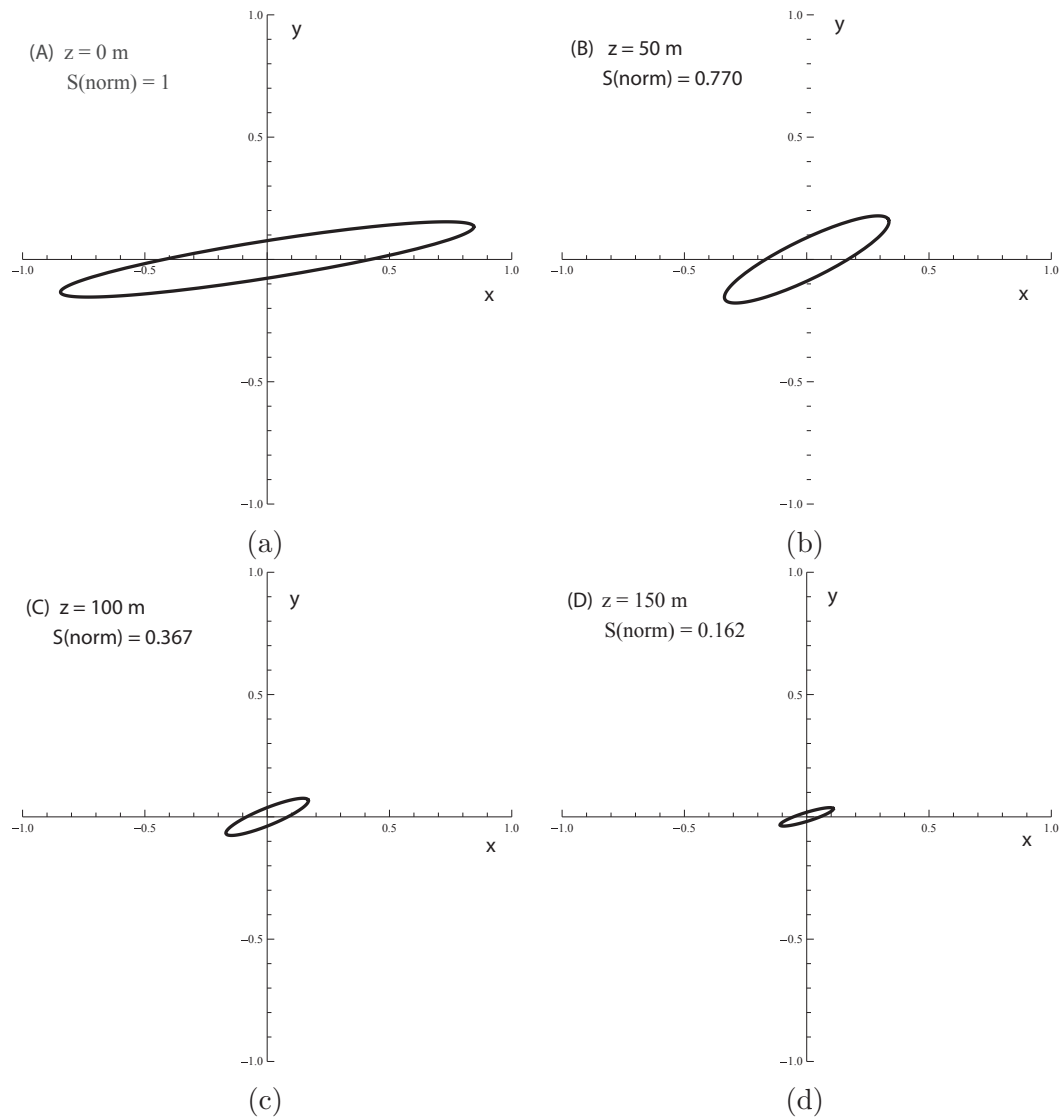
Figure 5.2: Typical evolution of the polarization ellipse of a stochastic beam in oceanic turbulence (on-axis).

(a) Spectral Density $S$

(b) Degree of Polarization $P$

(c) Orientation Angle $\psi$

(d) Degree of Ellipticity $\epsilon$
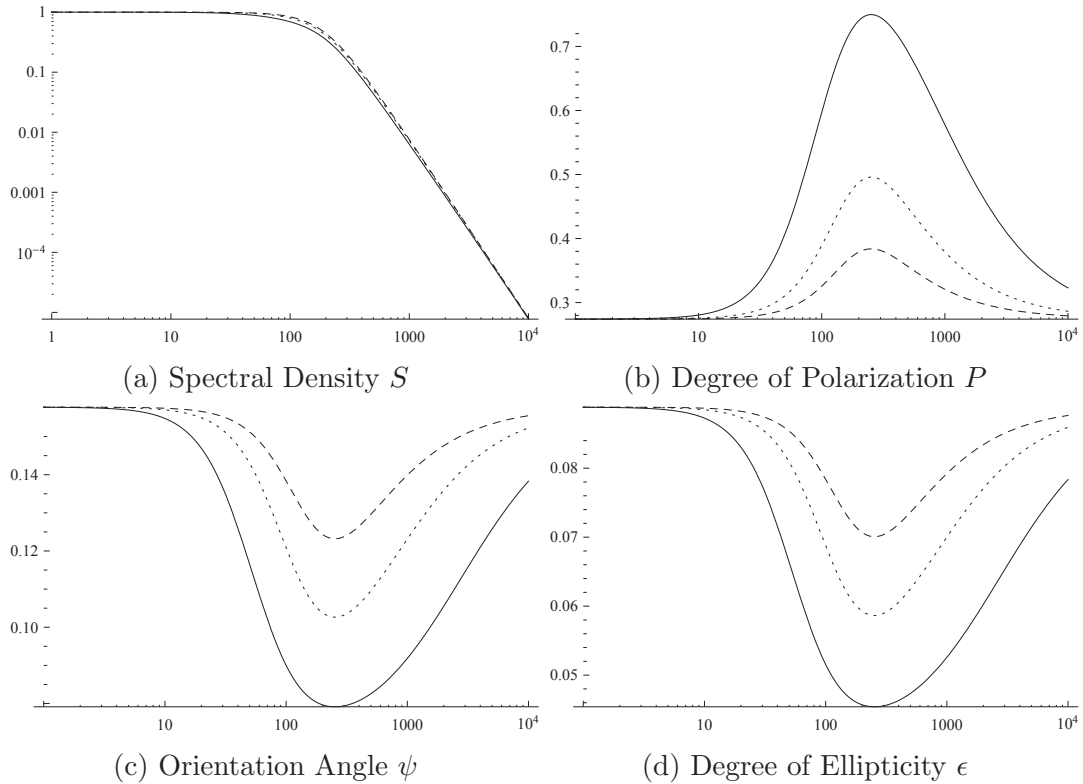
Figure 5.3: Variation of the statistical properties of the beam with distance $z$ (horizontal axis, in meters) for several values of the r.m.s. correlation coefficient $\delta_{xx}$ of the source.

change considerable and vary more drastically for smaller values of $\delta_{xx}$.

Figure 5.4 shows the dependence of the beam on the r.m.s source width $\sigma$ which in the figure takes values of $\sigma = 0.005m$ (solid curves) $\sigma = 0.01m$ (dotted curves), and $\sigma = 0.05m$ (dashed curves). In this case we do see a dependence of the spectral density on $\sigma$, being affected more for smaller values. Smaller $\sigma$ values also lead to larger changes in the polarization properties occurring closer to the source.

Figures 5.5 and 5.6 show the dependence of both the spectral density and polarization properties on the different oceanic turbulence parameters. Figure 5.5 shows the dependence on the parameter $\chi_T$ for values equal to $10^{-2}$ (solid curves), $10^{-6}$ (dotted curves), $10^{-10}$ (dashed curves). We have seen already that larger values of $\chi_T$

(a) Spectral Density $S$

(b) Degree of Polarization $P$

(c) Orientation Angle $\psi$

(d) Degree of Ellipticity $\epsilon$

Figure 5.4: Variation of the statistical properties of the beam with distance $z$ (horizontal axis, in meters) for several values of the r.m.s. width $\sigma$ of the source.

Figure 5.5: Variation of the statistical properties of the beam with distance $z$ (horizontal axis, in meters) for several values of the mean square temperature dissipation rate $\chi_T$.

correspond to stronger turbulence and that is apparent again in Figure 5.5. The larger values correspond to a larger decrease in spectral density occurring earlier along the propagation path, as well as significantly smaller changes in polarization properties of the beams. Indeed, when we take the extreme case of $\chi_T = 10^{-2}$ (solid curves), we see that all the polarization properties remain essentially constant along the propagation path. In this case, the extremely strong turbulence acts to suppress any polarization changes due to the source very early on in the propagation path. We have omitted explicitly showing the dependence on $\epsilon$ as again it will function similarly to that of $\chi_T$ albeit in an inverse way, i.e. larger values of $\varepsilon$ will give weaker turbulence as opposed to stronger.

(a) Spectral Density $S$

(b) Degree of Polarization $P$
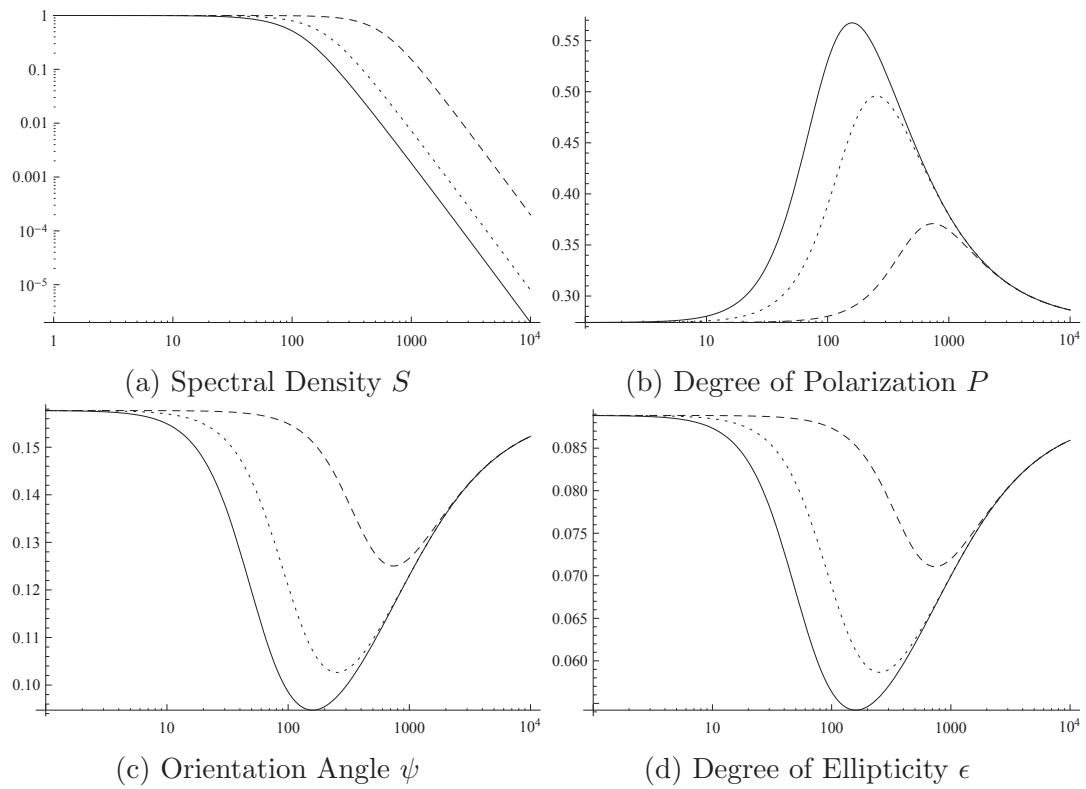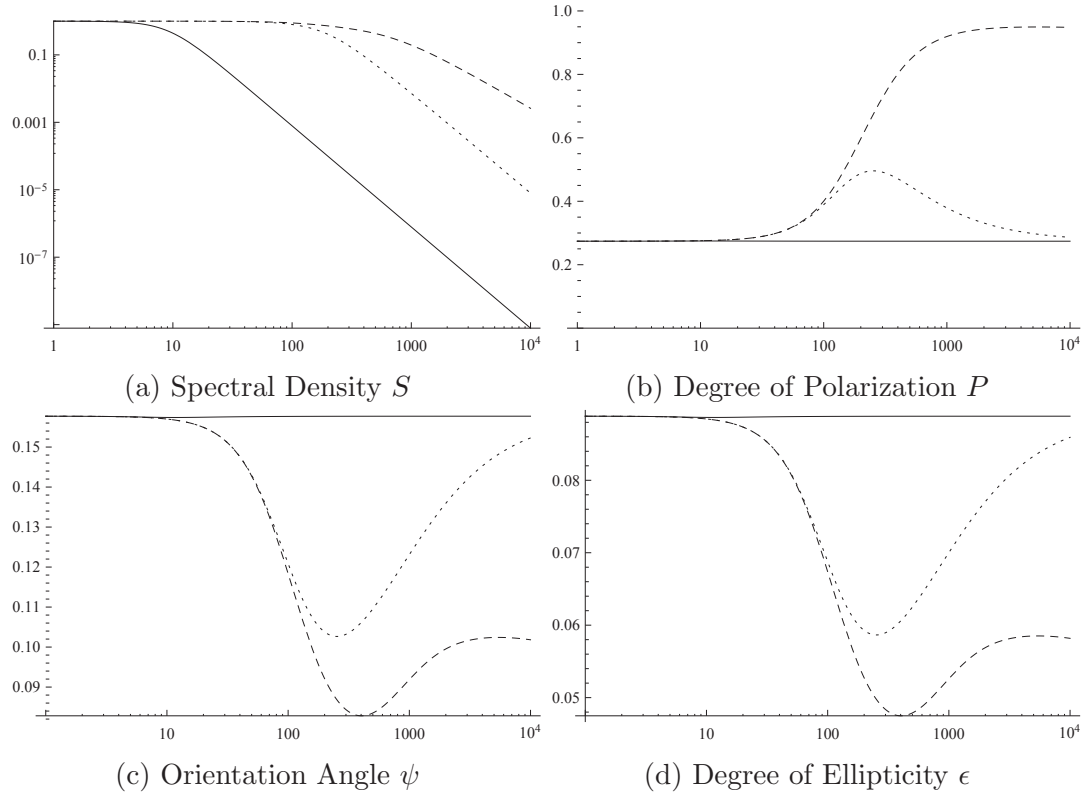
(c) Orientation Angle $\psi$

(d) Degree of Ellipticity $\epsilon$
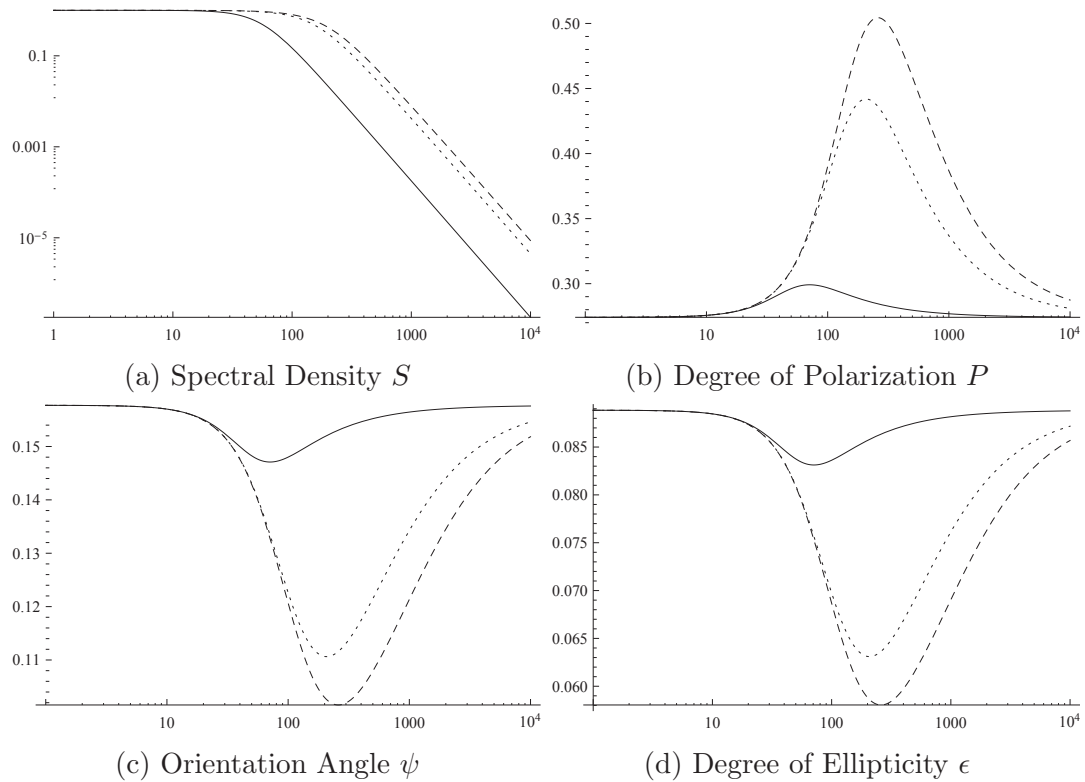
Figure 5.6: Variation of the statistical properties of the beam with distance $z$ (horizontal axis, in meters) for several values of the temperature-salinity balance parameter $w$.

Finally, Figure 5.6 shows the depends on the density ratio $w$. Here the values taken are $w = -0.1$ (solid curves), $w = -2.5$ (dotted curves), and $w = -4.9$ (dashed curves). We have seen in our analysis in Chapter 3, when $w$ takes values closer to 0, meaning a more salinity dominated turbulence, we have stronger turbulence. This trend continues here as the solid curves, $w = -0.1$ give us the fastest drop in spectral density as well as smaller changes in the polarization properties occurring closer to the source.

# Chapter 6

# Phase Screen Simulation of Oceanic Turbulence

In our investigation thus far in Chapters 2-5 we have taken a statistical approach using classic Rytov theory and the extended Huygens-Fresnel principle to study beam characteristics in oceanic turbulence theoretically. We will now use a numerical wave optics random phase screen simulation method to compare the results. Modeling of beam propagation in turbulence through the use of multiple computer-generated phase screens has been used for some time now [46]-[48]. The results of this technique are well documented in relation to atmospheric turbulence [49]-[50] and have been more recently used to study propagation of partially coherent beams [51]-[52]. As we have seen, analytical evaluation using the recent spatial power spectrum of refractive index fluctuations for the ocean given in [1] can be incredibly complex if feasible at all. The numerical wave optics simulation approach may therefore be preferable for certain situations as its calculations are not as complex.

In our simulation, we model the propagation of a wave through the ocean as the discrete case of propagation through a series of phase screens separated by free space as shown in Figure 6.1. This figure shows phase screens labeled $A_{(1)}, A_{(2)}, ..., A_{(n)}$ each separated by an equal distance of free space as well as the propagation path of the beam. This situation, where the continuous random medium is broken up into a series
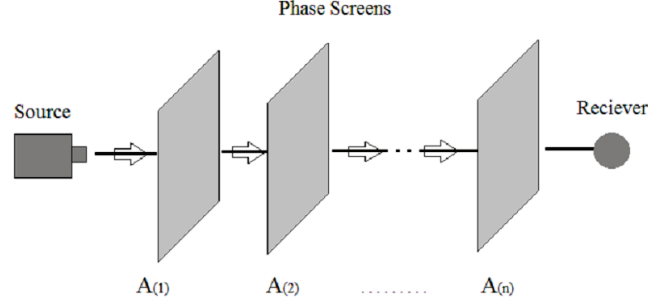
Figure 6.1: Graphic representation of the geometry used in simulating propagation via numerical phase screen approach.

of independent slabs, each representing weak turbulence on its own, is equivalent to the Markov approximation used in analytical studies [54]. To propagate the beam along this path we will need to alternate between sections of free space propagation, and passage through a thin phase screen whose characteristics are defined by the spatial power spectrum $\Phi_N$.

The propagation through the sections of free space is accomplished through the Huygens-Fresnel integral [55]

$$U(\mathbf{r}, L, \lambda) = -2ik \iint_{-\infty}^{\infty} G(\boldsymbol{\rho}, \mathbf{r}, L)U_0(\boldsymbol{\rho}, 0)d^2\rho, \tag{6.1}$$

where $U_0(\boldsymbol{\rho}, 0)$ is the optical field in the source plane, $k$ is the wave number, and $G(\boldsymbol{\rho}, \mathbf{r}, L)$ is the free-space Greens function given by

$$G(\boldsymbol{\rho}, \mathbf{r}, L) = \frac{1}{4\pi L} \exp[ikL + \frac{ik}{2L}|\boldsymbol{\rho} - \mathbf{r}|^2]. \tag{6.2}$$

For practical purposes, it will be convenient to recognize that equation 6.1 has the

form of a two dimensional Fourier transform, allowing us to write it as [56]

$$U(\mathbf{r}, L, \lambda) = \mathbf{F}^{-1}[\mathbf{F}(U_0(\boldsymbol{\rho}, 0, \lambda))H(\kappa)], \tag{6.3}$$

where here $\kappa$ is the spatial frequency, $\mathbf{F}$ is the Fourier Transform, and $\mathbf{F}^{-1}$ is the inverse Fourier transform. $H(\kappa)$ is the free space propagation transfer function given by [57]

$$H(\kappa) = \exp[i\pi L(\frac{2}{\lambda} - \lambda\kappa^2)]. \tag{6.4}$$

We will use this process to propagate the beam through the sections of free space that fall between the phase screens created to model the turbulence. The passage through the $n^{th}$ phase screen at position z is done simply by

$$U_{n+}(\mathbf{r}, z^+, \lambda) = U_{n-}(\mathbf{r}, z^-, \lambda)\exp[-i\theta(\mathbf{r})], \tag{6.5}$$

where $\theta(\mathbf{r})$ is the turbulence induced phase whose generation is outlined in the following section.

## 6.1 Phase Screen Generation

In order to pass the beam through this system of phase screens we first need to generate phase screens that have the same properties as the random medium we desire. For our purposes, we require the same statistics as that of the refractive-index power spectrum given in equation 1.6. We begin again by making the assumptions of statistically homogeneous and isotropic turbulence and we assume that no amplitude

change occurs when the beam passes through a phase screen, that is, each screen introduces an independent random contribution to the phase only. To relate back to our refractive-index spectrum $\Phi_n$ we begin by specifying the statistics of a single phase screen. We see that we can write the phase correlation function as [47]

$$B_\theta(\boldsymbol{\rho_1}, \boldsymbol{\rho_2}) = k^2 \iint_0^{\delta_z} \langle n(\boldsymbol{\rho_1}) n(\boldsymbol{\rho_2}) \rangle d^2\rho, \tag{6.6}$$

where here $\boldsymbol{\rho_1}$ and $\boldsymbol{\rho_2}$ are vectors in the plane of the phase screen, $B_\theta$ is the correlation between the phases arriving at two points, and $n(\boldsymbol{\rho_1})$ is the refractive index at point $\boldsymbol{\rho_1}$. We can write the correlation function of refractive index variation as

$$\langle n(\boldsymbol{\rho_1}) n(\boldsymbol{\rho_2}) \rangle = A_n(\boldsymbol{\rho_1} - \boldsymbol{\rho_2}). \tag{6.7}$$

It can also be shown that the correlation of refractive-index fluctuations is related to the spatial power spectrum $\Phi_n$ as [54]

$$A_n(\boldsymbol{\rho}) = 2\pi \iint_{-\infty}^{\infty} \Phi_n(\kappa) exp[i\kappa \cdot \boldsymbol{\rho}] d^2\kappa. \tag{6.8}$$

This gives us a relationship between the phase spectrum and the refractive index spectrum of

$$\Phi_\theta(\kappa) = 2\pi k^2 \delta_z \Phi_n(\kappa). \tag{6.9}$$

We are now able to construct a phase screen, denoted $\theta$ using the well-known method using Gaussian noise to create a random phase screen with the same statistics as the

random media we desire [48],[58]. Each individual phase screen is given by

$$\theta(j\Delta x, l\Delta y) = \sum_{n=0}^{N_x} \sum_{m=0}^{N_y} [a(n,m) + ib(n,m)] \times exp[2\pi i(jn/N_x + lm/N_y)]. \qquad (6.10)$$

Here $N_x$ and $N_y$ are the dimensions of each phase screen, $\Delta_x$ and $\Delta_y$ are the grid spacings in the x and y coordinates, and $a(n,m)$ and $b(n,m)$ are zero-mean Gaussian random numbers with

$$\langle a^2(n,m) \rangle = \langle b^2(n,m) \rangle = \Delta q_x \Delta q_y \Phi_\theta(\kappa), \qquad (6.11)$$

where $\Delta q_x = 2\pi/(N_x \Delta x)$ and $\Delta q_y = 2\pi/(N_x \Delta y)$ are the grid size of the simulation in spectral space. Inserting the spectrum for oceanic turbulence $\Phi_n$ from equation 1.6 into equation 6.9 and then into equation 6.10 gives us the desired phase screens with the same statistics of the oceanic turbulence we intend to study. Figure 6.2 shows several different typical phase screens generated for differing oceanic turbulence parameters using the above method. The color difference from white to black signifies a phase difference running from 0 to $2\pi$.

## 6.2 Simulation Results

In the results that follow, each plot shows the result of 16 phase screens placed at even intervals along the propagation path. Each phase screen, as well as the source plane contain 512x512 points of analysis and have square sides 10cm in length. Unless otherwise specified, all the parameters are identical to those used in Chapter 3,
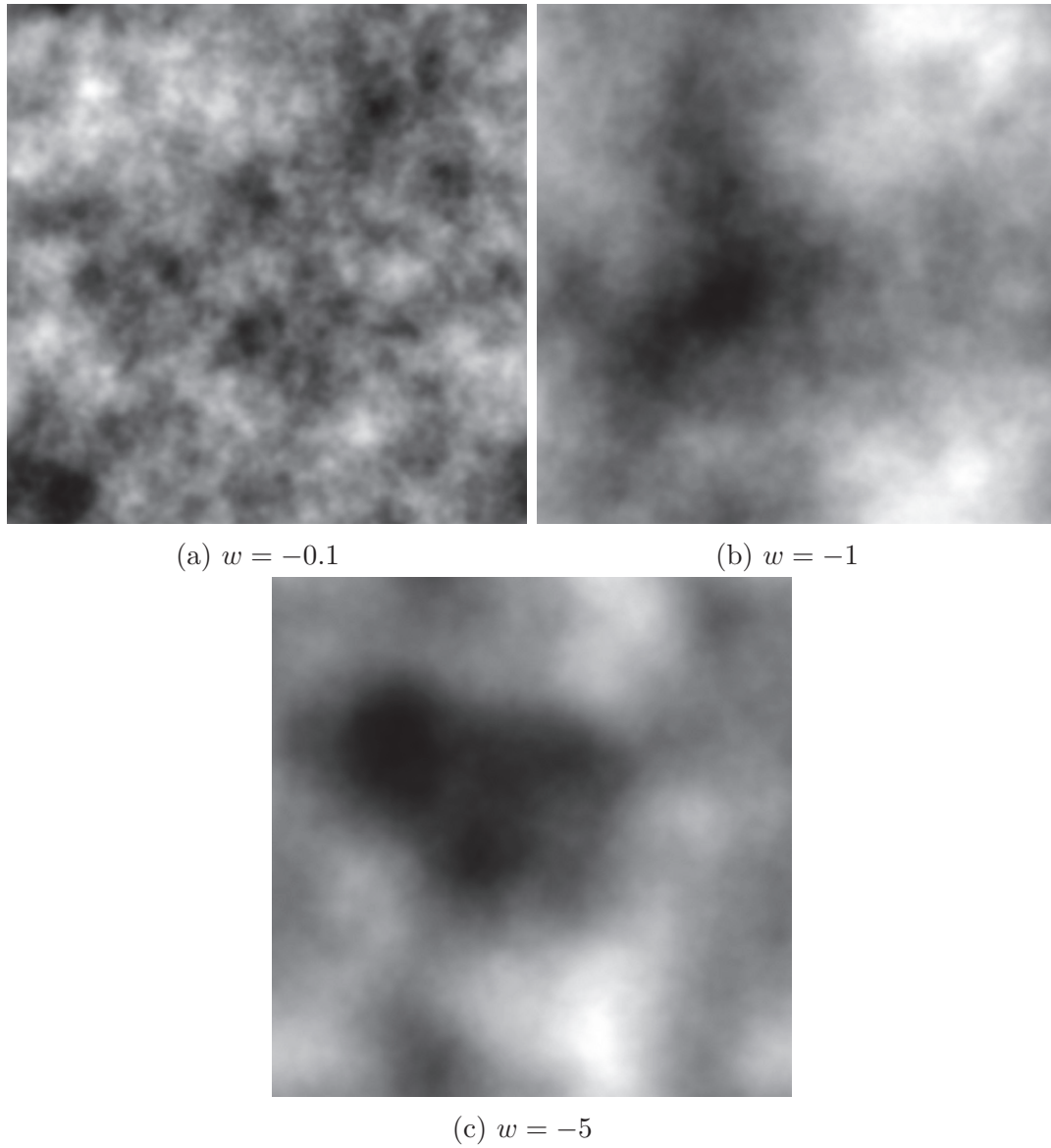
(a) $w = -0.1$
(b) $w = -1$

(c) $w = -5$

Figure 6.2: Typical phase screens for different values of the density gradient ratio $w$. All screens are for propagation distances of 1 meter, with $\chi_T = 10^{-7}$ and $\epsilon = 10^{-5}$.

including beginning with a unit amplitude Gaussian source, so that direct comparisons may be made. In particular, we choose a wavelength of $\lambda = 0.417 \times 10^{-6}$m, an initial beam size of $W_0 = 0.01$m, $\chi_T = 10^{-7}\frac{m^2}{s^3}$, and $\varepsilon = 10^{-5}\frac{K^2}{s}$. Figure 6.3 shows the intensity distribution in the source plane, as well as the observation plane of both a single realization, and for an average of 2000 realizations after propagation of 30 meters with a $w$ parameter equal to $-0.2$ to show the effects of the turbulence. In the plots following this, we will be interested in average statistics of the beam at the receiver, and thus we choose to average a total of 2000 realizations to get accurate results. The opinion in the literature about the correct number of realizations to average to ensure reliable results for both intensity and scintillation properties is varied. Some suggest 100 realizations is enough [59], several find that 500 realizations is sufficient ([56], [60], [61], while another prefers 2000 [62]. We have chosen 2000 in what follows to ensure reliable results.

Figure 6.4 shows the intensity profiles averaged over 2000 realizations for several propagation lengths and values of the density gradient ratio $w$. As expected, these plots show the now familiar trend of salinity dominant fluctuations, that is $w$ closer to 0, giving high beam degradation over the same propagation length as compared to temperature dominant fluctuations, as $w$ approaches $-5$. These figures can be directly compared to Figure 3.5 and we see that they agree quite well. In the case of $w = -0.2$ we see that the values found using the multiple phase screen approach are slightly lower than those found using Rytov theory along with the method of effective beam parameters in Chapter 3. On the contrary, when $w = -1$ and $w = -2$ we find slightly higher values using multiple phase screens. This slight discrepancy between
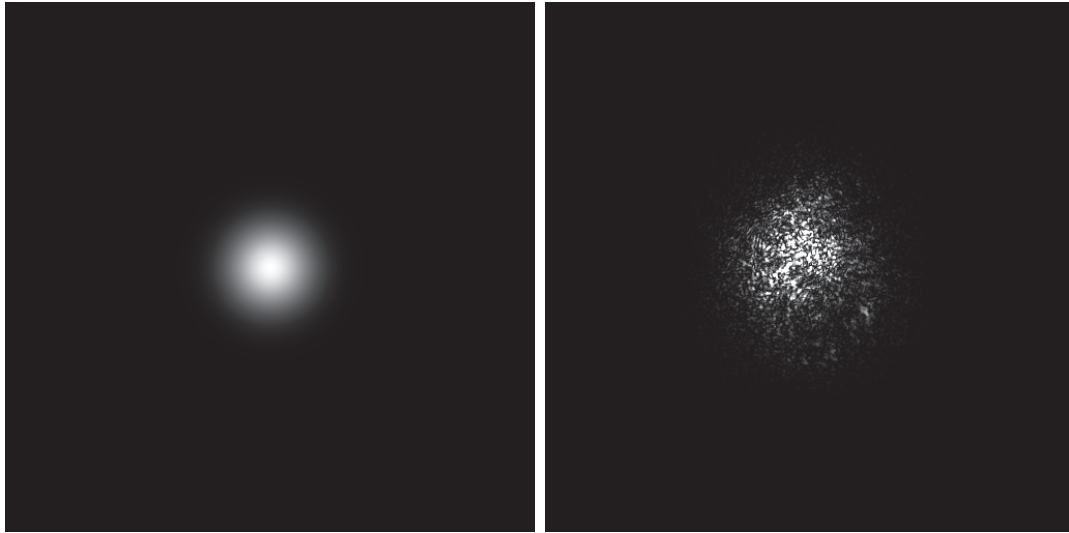
(a) Source Intensity

(b) Intensity of one realization after 30 meters of propagation with $w = -0.2$
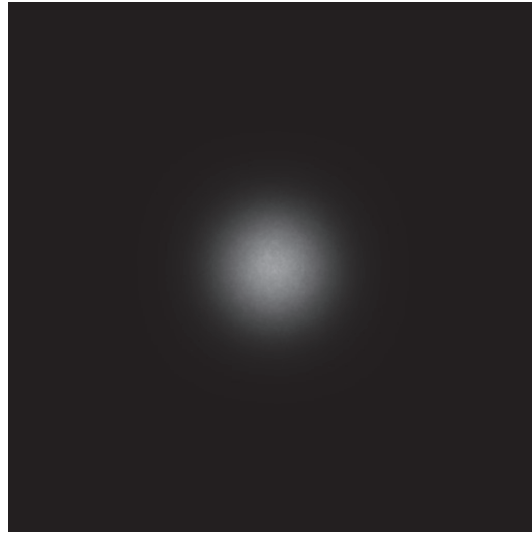
(c) Averaged intensity of 2000 realizations after 30 meters of propagation with $w = -0.2$

Figure 6.3: Intensity profiles of both the source plane, as well as the observation plane after propagation of 30 meters with $w = -0.2$

the two methods is to be expected as both methods use some assumptions that could cause slight differences in practice. On the large part we see very good agreement between the two methods.

Figures 6.5 and 6.6 display the scintillation properties for a Gaussian beam. In these figures we have calculated the scintillation using [11]

$$\sigma_I^2(\mathbf{r}, L, \lambda) = \frac{\langle I^2(\mathbf{r}, L, \lambda)\rangle - \langle I(\mathbf{r}, L, \lambda)\rangle^2}{\langle I(\mathbf{r}, L, \lambda)\rangle^2}, \tag{6.12}$$

where the average is over the 2000 propagation realizations. In Figure 6.5, we see typical scintillation profiles across the beam for propagation distances of 30m and 70m with $w = -1$. We have omitted the 10m propagation image as, as we will see in Figure 6.6, it is very flat across the beam area. This feature, as well as the appearance of both images in Figure 6.5 can be explained by the trend highlighted in Figure 3.4. We see that at short propagation distances, as in the 10m case, the scintillation index on the beam center is almost equivalent to that on the beam edge. This gives us the almost flat profile for scintillation for all the cases of 10m propagation. In the case of 30 and 70 meters of propagation we begin to see the trend of the beam edge having much higher scintillation than on the beam center.

Figure 6.6 shows the scintillation profile across the beam cross section for the usual three values of the density gradient ratio $w = -0.2$, $w = -1$, and $w = -2.0$ for three different propagation distances. The most notable difference from the expected occurs in Figure 6.6a, where the scintillation values of 30m exceed that of 70m. The other cases studied follow the expected trend of stronger turbulence and longer
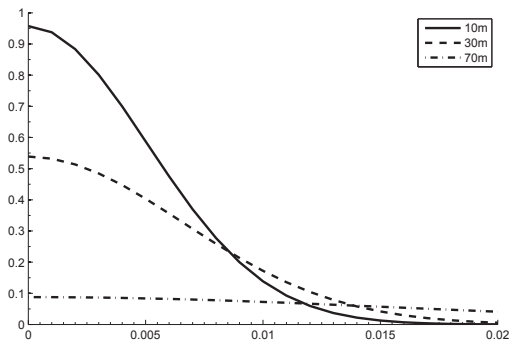
(a) $w = -0.2$
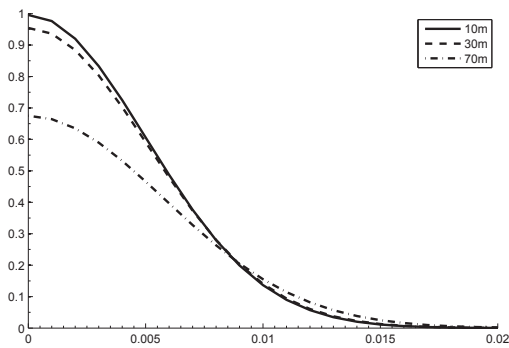


(b) $w = -1$
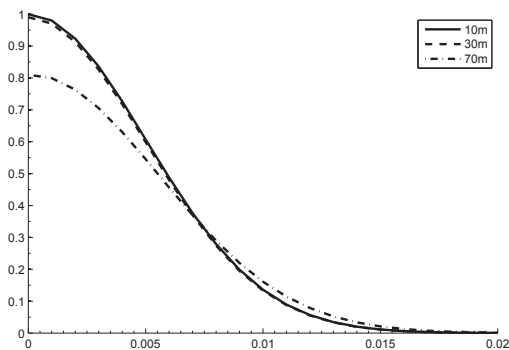


(c) $w = -2$

Figure 6.4: Intensity profiles as calculated via multiple phase screen approach of a Gaussian beam for several propagation lengths and $w$ values. All plots have $\chi_T = 10^{-7}\frac{m^2}{s^3}$, $\varepsilon = 10^{-5}\frac{K^2}{s}$, $L = 10m$ (solid curve), $L = 30m$ (dashed curve), and $L = 70m$ (dot-dashed curve).
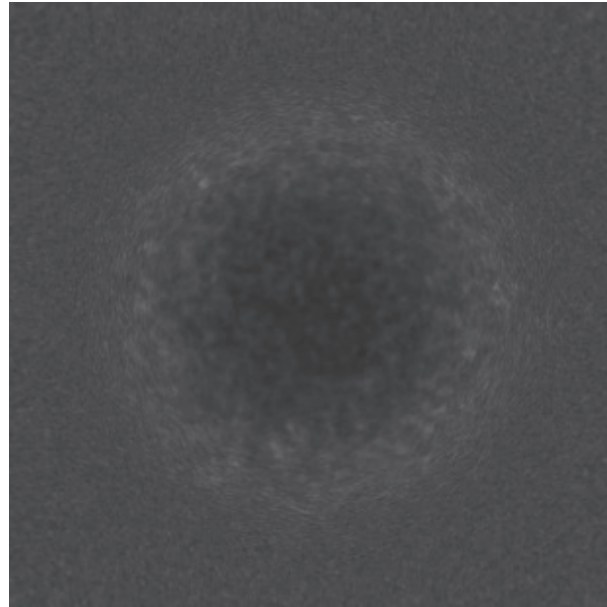
(a) $L = 30m$
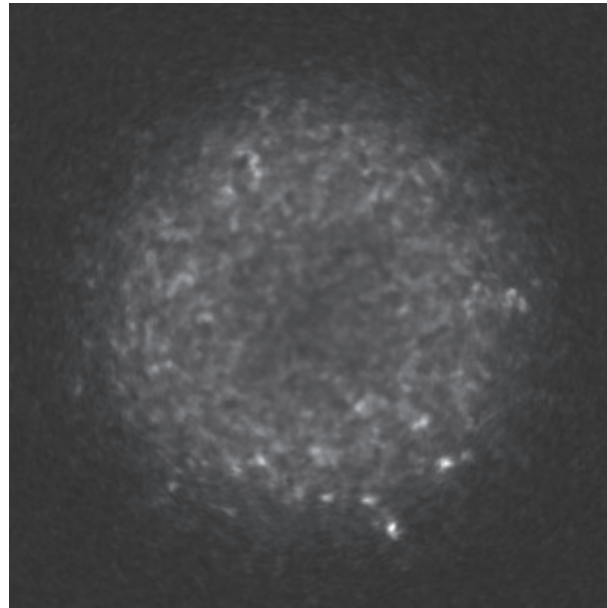


(b) $L = 70m$

Figure 6.5: Scintillation profiles across the beam area. Images have $\chi_T = 10^{-7} \frac{m^2}{s^3}$, $\varepsilon = 10^{-5} \frac{K^2}{s}$ and $w = -1$.

propagation distances leading to higher scintillation values. Due to the incredibly strong nature of the turbulence after 70 meters of propagation with $w = -0.2$, the beam is degraded by such extreme amounts, as highlighted in the intensity profiles of both Figures 3.5 and 6.4 for the 70 meter propagation path, that it no longer keeps the same scintillation trends. The extreme turbulence has taken the intensity profile from Gaussian in nature, to almost flat across the area. The combination of an almost flat intensity profile, along with the very low absolute intensities, allow for the scintillation reduction from the 30 meter to 70 meter case.

Aside from this one outlying case, we see that the other plots follow exactly the trends outlined in Figure 3.4. For the initial beam size of 1 centimeter we have chosen, the three propagation distances 10, 30, and 70 meters correspond to values of the Fresnel ratio $\Lambda_0 = \frac{2L}{kW_0^2}$ used in Figure 3.4 of 0.0133, 0.0398, and 0.0929 respectively. At these values we will not see the ratio of scintillation on the beam edge to the beam center approach the values of 20 or higher possible with a Fresnel ratio of 1, but we do find similar ratios to those predicted in Figure 3.4. At 10 meters of propagation, or $\Lambda_0 = 0.0133$ we expect the beam edge to be approximately equal to that of the beam center, and we find that for all three $w$ values. After 70 meters of propagation, $\Lambda_0 = 0.0929$ we expect a ratio of approximately $3.5 - 4$ which is only slightly larger than what we have found in practice for $w = -1$ and $w = -2$. Overall, the form of the scintillation profiles seen using the multiple phase screen approach agree with those found in Chapter 3 using the extended Rytov theory.
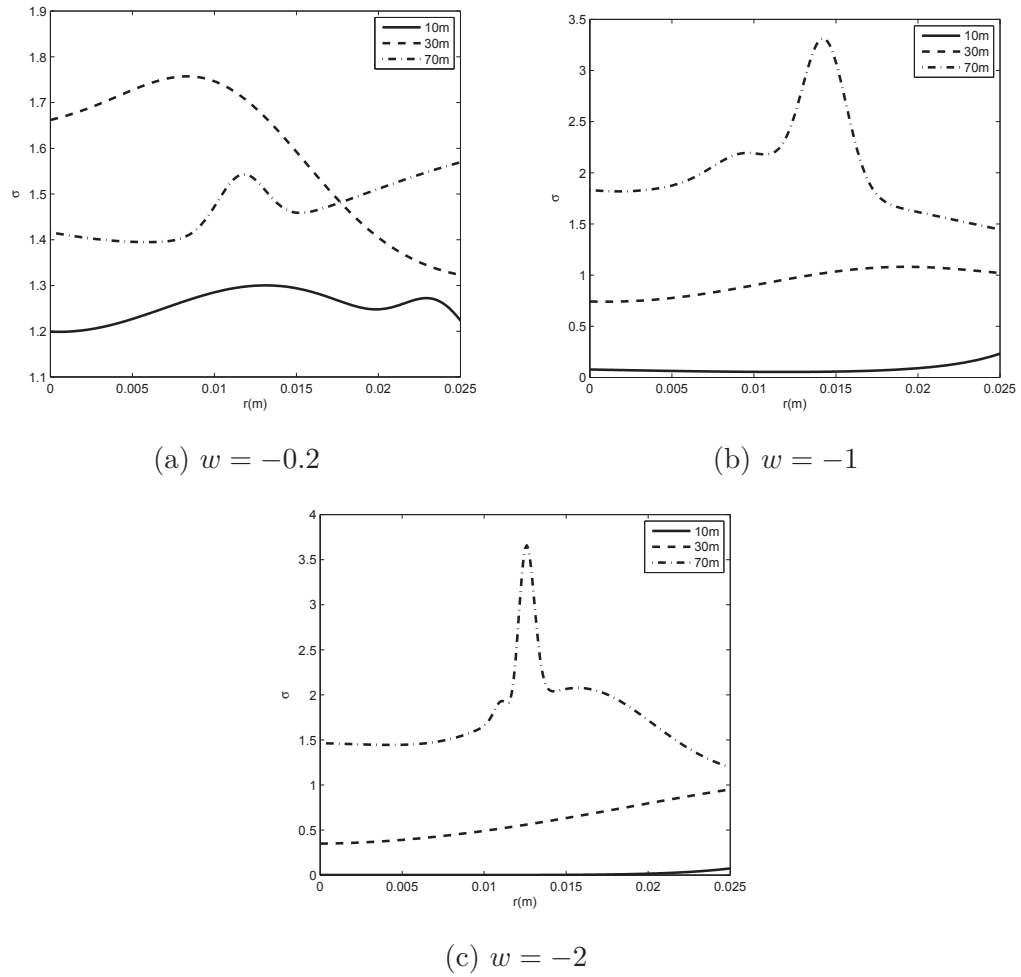
(a) $w = -0.2$

(b) $w = -1$

(c) $w = -2$

Figure 6.6: Scintillation values vs. radial distance from the beam center in meters for several values of $w$ and propagation distance $L$. Other parameters have the same values as in Figure 6.5

# Chapter 7

# Conclusions

Throughout the text we have explored many critical properties of an optical beam propagating through oceanic turbulence with the aid of a new and more complete model for the random fluctuations in the index of refraction of the ocean [1]. Applications such as remote sensing, laser radar links, as well as wireless communication channels all will benefit from this study. Due to the complicated and expensive nature of setting up optical networking equipment underwater, it is crucial to have a solid theoretical understanding of the environment we want to work in beforehand. The text studies a range of some of the more widely studied beam sources including a fully coherent Gaussian beam, a partially coherent scalar Gaussian Schell-model beam, as well as a partially coherent electromagnetic Gaussian Schell-model source. Several approaches to calculating statistics are used and the results are compared to find a very good agreement between the classic Rytov theory and the numerical wave optics approach through the use of multiple phase screens.

The inclusion of the both salinity and temperature fluctuations to the spectrum of fluctuations of the refractive index is essential in an accurate study of the oceanic environment. We have shown that when salinity fluctuations dominate, much stronger

turbulence is created. Studies using only temperature fluctuations for the ocean neglect this effect and cannot account for its impact. We have seen throughout the text the importance of its inclusion in all beam properties from intensity and coherence, to polarization and spectral shift.

We have found that in general, beam statistics including spectral shift and polarization properties behave in much the same way, qualitatively, as that found in atmospheric turbulence, albeit occurring at much shorter propagation distances in the ocean. Many of the trends seen occur at propagation distances as much as two or three orders of magnitude smaller in the ocean. We have also shown that for certain cases, beam intensity degradation due to optical turbulence alone can contribute equally, or even more so than that of absorption showing the importance of considering the optical turbulence for all practical uses.

The results presented here establish a solid foundation for much future work in the area of optical beam propagation in oceanic turbulence. Further studies are continually being produced that follow from the basis outlined in this text including work on the wave structure function [63], as well as work on other, less widely studied beam sources [64],[65]. As with the much wider studied atmospheric turbulence, further study may prove fruitful in establishing classes of beam sources that prove more robust while propagating through oceanic turbulence. Additional studies on bit error rate of a communication channel, enhanced backscatter in laser radar systems, as well as the inclusion of particulate scattering [66] can all be done as an extension of the work presented here.

# References

[1] V. V. Nikishov and V. I. Nikishov, "Spectrum of turbulent fluctuation of the sea–water refractive index", *Int. J. Fluid Mech. Res.* **27**, 82-98 (2000).

[2] Garry L. Brown and Anatol Roshko, "On density effects and large structure in turbulent mixing layers" *J. Fluid Mech.* **64** 775-816 (1974).

[3] A. N. Kolmogorov, "The local structure of turbulence in an incompressible viscous fluid for very large reynolds numbers," *C. R. Acad. Sci. U.S.S.R.* **30**,301-305 (1941).

[4] F. H. Champagne, C. A. Friehe, J. C. LaRue, and J. C. Wyngaard, "Flux measurements, flux-estimation techniques, and fine-scale turbulence measurements in the unstable surface layer over land", *J. Atmosp. Sci.* **34**, 515-530 (1977).

[5] R.J. Hill, "Optical propagation in turbulent water," *J. Opt. Soc. Am.* **68**, Issie 8, 1067-1072 (1978).

[6] Frank Hanson and Mark Lasher, "Effects of underwater turbulence on laser beam propagation and coupling into single mode optical fiber" *Appl. Opt.* **49**, 3224-3230 (2010).

[7] S. A. Thorpe, *An Introduction to Ocean Turbulence* (Cambridge University Press, 2007).

[8] S. A. Thorpe, *The Turbulent Ocean*, (Cambridge University Press, 2005).

[9] A. E. Gargett, W. J. Merryfield, and G. Holloway, "Direct numerical simulation of differential scalar diffusion in three-dimensional stratified flow" *Journal of Physical Oceanography* **33**, 1758-1782 (2003).

[10] P. R. Jackson, and C. R. Rehmann, "Laboratory measurements of differential diffusion in a diffusively stable, turbulent flow", *J. Physical Oceanography* **33**, 1592-1603 (2003).

[11] L. C. Andrews, R. L. Phillips, *Laser Beam Propagation Through Random Media*, (SPIE press, Bellington, 2005).

[12] S. M. Rytov, "Diffraction of light by ultrasonic waves," *Bulletin of the Academy of Sciences of the USSR, Physical Series* **2**, 223-259 (1937).

[13] A. M. Obukhov, "Effect of weak inhomogeneities in the atmosphere on sound and light propagation," *Izv. Acad. Nauk SSSR, Ser. Geofiz.* **2**, 155-165 (1953).

[14] M. S. Belen'kii, V. L. Mirinov, "Coherence of the field of a laser beam in a turbulent atmosphere," *Sov. J. Quant. Electron.* **10**,595-597 (1980)

[15] M. S. Belen'kii, V. L. Mirinov, "Mean diffracted rays of an optical beam in a turbulent medium," *J. Opt. Soc. Am.* **70**, 159-163 (1980)

[16] R.M. Pope, E.S. Fry, "Absorption spectrum (380700 nm) of pure water. II. Integrating cavity measurements", *Applied Optics* **36**, 8710-8723 (1997).

[17] Korotkova, O., N. Farwell, and E. Shchepakina. "Light scintillation in oceanic turbulence." *Waves in Random and Complex Media* **22** 260-266 (2012).

[18] Farwell, N., and O. Korotkova. "Intensity and coherence properties of light in oceanic turbulence." *Optics Communications* **285** 872-875 (2012).

[19] E. Wolf, *Introduction to theories of coherence and polarization of light*, Cambridge University Press, 2007.

[20] G. Gbur and E. Wolf, "Spreading of partially coherent beams in random media," *J. Opt. Soc. Am. A* **19**, 1592-1598 (2002).

[21] T. Shirai, A. Dogariu, E. Wolf, "Mode analysis of spreading of partially coherent beams propagating through atmospheric turbulence," *J. Opt. Soc. Am. A* **20**, 1094-1102 (2003).

[22] W. Lu, L. Liu, J. Sun, Q. Yang, Y. Zhu, "Change in degree of coherence of partially coherent electromagnetic beams propagating through atmospheric turbulence", *Opt. Commun.* **271**, 1-8 (2007).

[23] D. F. V. James, "Change of polarization of light beams on propagation in free space" *J. Opt. Soc. Am. A* **11**, 1641-1643 (1994).

[24] F. Gori, M. Santarsiero, G. Piquero, R. Borghi, A. Mondello, R. Simon, "Partially polarized Gaussian Schell-model beams", *J. Opt. Pure Appl. Opt.* **3**, 1-9 (2001).

[25] S. R. Seshadri, "Partially coherent Gaussian Schell-model electromagnetic beams", *J. Opt. Soc. Am. A* **16**, 1373-1380 (1999).

[26] S. R. Seshadri, "Polarization properties of partially coherent Gaussian Schell-model electromagnetic beams", *J. Appl. Phys.* **87**, 4084-4093 (2000).

[27] O. Korotkova, M. Salem and E. Wolf, "The far-zone behavior of the degree of polarization of partially coherent beams propagating through atmospheric turbulence", *Opt. Comm.* **233**, 225-230 (2004).

[28] M. Salem, O. Korotkova, A. Dogariu and E. Wolf, "Polarization changes in partially coherent EM beams propagating through turbulent atmosphere", *Waves in Random Media* **14**, 513-523 (2004).

[29] L. Mandel and E. Wolf, *Optical Coherence and Quantum Optics*, Cambridge University Press, 1995.

[30] H. Roychowdhury and O. Korotkova, "Realizability conditions for electromagnetic Gaussian Schell-model sources", *Opt. Comm.* **249**, 379-385 (2005).

[31] O. Korotkova, M. Salem and E. Wolf, "Beam conditions for radiation generated by an electromagnetic Gaussian Schell-model source", *Opt. Lett.* **29**, 1173-1175 (2004).

[32] D. Goldstein, *Polarized Light*, Second Ed., Marcel Dekker, 2003.

[33] O. Korotkova and N. Farwell, "Effect of oceanic turbulence on polarization of stochastic beams", *Opt. Comm.* **284**, 1740-1746 (2011).

[34] O. Korotkova, M. Salem, A. Dogariu and E. Wolf, "Changes in the polarization ellipse of random electromagnetic beams propagating through turbulent atmosphere", *Waves in Random and Complex Media* **15**, 353-364 (2005).

[35] W. Gao, "Propagation of degree of polarization of a random electromagnetic beam propagating through tissue", *Opt. Comm.* **260**, 749-756 (2006).

[36] W. Gao and O. Korotkova, "Changes in the state of polarization of a random electro-magnetic beam propagating through tissue", *Opt. Comm.* **270**, 474-478 (2007).

[37] E. Wolf, "Invariance of the spectrum of light on propagation," *Phys. Rev. Lett.* **56**, 1370-1372 (1986).

[38] O. Korotkova, J. Pu, E. Wolf, "Spectral changes in electromagnetic stochastic beams propagating through turbulent atmosphere," *J. Mod. Opt.* **55**, 1199-1208 (2008).

[39] O. Korotkova, E. Shchepakina, "Color changes in stochastic light fields propagating in non-Kolmogorov turbulence," *Opt. Lett.* **35**, 3772-3774 (2010).

[40] W. Gao, "Spectral changes of the light produced by scattering from tissue," *Opt. Lett.* **35**, 862-864 (2010).

[41] Jerry D. Gibson [Ed.], *The Communications Handbook* (CRC Press, 2002).

[42] J.B. Campbell, *Introduction to Remote Sensing* (Taylor and Francis, Fourth Edition, 2007).

[43] G. Gbur, E. Wolf, "Spreading of partially coherent beams in random media," *J. Opt. Soc. Am. A* **19**, 1592-1598 (2002).

[44] Z. Tong, S. Sahin and O. Korotkova, "Sensing of semi-rough targets embedded in atmospheric turbulence by means of stochastic electromagnetic beams", *Opt. Comm.* **283**, 4512-4518 (2010).

[45] N. Farwell, E. Shchepakina, and O. Korotkova, "Spectral changes in light beams propagating in oceanic turbulence", *Appl. Phys. B*, in press (2011).

[46] C. Macaskill and T.E.Ewart, " Computer simulation of two-dimensional random wave propagation," *IMA J. Appl. Math.* **33**, 1-15 (1984).

[47] J.M. Martin and S.M.Flatte, "Intensity images and statistics from numerical simulation of wave propagation in 3-D random media," *Appl. Opt.* **27**, 2111-2126 (1988).

[48] D. L. Knepp, "Multiple phase-screen calculation of the temporal behavior of stochastic waves," *Proc. IEEE* **71**, 722 (1983).

[49] D.H.Nelson, D.L.Walters, E.P. MacKerrow, M.J. Schmitt, C.R. Quick, W.M. Porch, and R. R. Petrin, "Wave optics simulation of atmospheric turbulence and reflective speckle effects in CO2 lidar," *Appl. Opt.* **39**, 1857-1871 (2000).

[50] A. Belmonte, "Feasibility study for the simulation of beam propagation: consideration of coherent lidar performance," *Appl. Opt.* **39**, 5426-5445 (2000).

[51] X. Xiao and D. Voelz, "Wave optics simulation approach for partial spatially coherent beams," *Opt. Express* **14**, 6986-6992 (2006).

[52] X. M. Qian, W. Y. Zhu, A. T. Wang, C. Gu, and R. Z. Rao, "Numeric simulation for coherent and partially coherent beam propagation through atmospheric turbulence," *Chin. Phys. Lett.* **27**, 044214 (2010).

[53] Wm. A. Coles, J. P. Filice, R. G. Frehlich, and M. Yadlowsky "Simulation of wave propagation in three-dimensional random media" *Appl. Opt.* **34**, 2089-2101 (1995).

[54] V. I. Tatarskii, *The Effects of the Turbulent Atmosphere on Wave Propagation* (National Technical Information Service, Springfield, Va., 1971).

[55] J.W. Goodman *Introduction to Fourier Optics* (McGraw-Hill, New York, 1968).

[56] D. Voelz, *Computational Fourier Optics a MATLAB Tutorial*, (SPIE, 2011).

[57] H. T. Eyyuboglu, D. Voelz, and X. Xiao, "Scintillation analysis of truncated Bessel beams via numerical turbulence propagation simulation" *Appl. Opt.* **52**, 8032-8039 (2013).

[58] Rod Frehlich "Simulation of laser propagation in a turbulent atmosphere," *Appl. Opt.* **39**, 393-397 (2000).

[59] X. Liu and J. Pu, "Investigation on the scintillation reduction of elliptical vortex beams propagating in atmospheric turbulence," *Opt. Express* **19**, 26444-26450 (2011).

[60] A. Belmonte, "Feasibility study for the simulation of beam propagation: consideration of coherent lidar performance," *Appl. Opt.* **39**, 5426-5445 (2000).

[61] W. Cheng, J. H. Haus, and Q. Zhan, "Propagation of vector vortex beams through a turbulent atmosphere," *Opt. Express* **17**, 17829-17836 (2009).

[62] X. Qian, W. Zhu, and R. Rao, "Numerical investigation on propagation effects of pseudo-partially coherent Gaussian Schell-model beams in atmospheric turbulence," *Opt. Express* **17**, 3782-3791 (2009).

[63] Yalcin Ata and Yahya Baykal, "Structure functions for optical wave propagation in underwater medium", *Waves in Random and Complex Media* **24**, 164-173 (2014).

[64] Xu, Jia, and Daomu Zhao. "Propagation of a stochastic electromagnetic vortex beam in the oceanic turbulence." *Optics & Laser Technology* **57**, 189-193 (2014).

[65] Fu, Wenyu, and Hanmou Zhang. "Polarization changes in a partially coherent radially polarized doughnut beam through turbulent ocean." *Journal of Modern Optics* **60** 1576-1584 (2013).

[66] Zhisong Tong and Olga Korotkova, "Technique for interaction of optical fields with turbulent medium containing particles," *Optics Letters* **36**, 3157-3159 (2011).